UNDERSTANDING THE CIRCUMGALACTIC MEDIUM THROUGH

ARCHIVAL SPECTROSCOPIC STUDIES

BY

NIGEL LAWRENCE MATHES, B.S., M.S.

A dissertation submitted to the Graduate School

in partial fulfillment of the requirements

for the degree

Doctor of Philosophy

Major Subject: Astronomy

New Mexico State University

Las Cruces New Mexico

July 2017

"Understanding the Circumgalactic Medium Through Archival Spectroscopic Studies," a dissertation prepared by Nigel L. Mathes in partial fulfillment of the requirements for the degree, Doctor of Philosophy, has been approved and accepted by the following:

_____

Lou-Vicente Reyes, PhD
Dean of the Graduate School

_____

Christipher W. Churchill
Chair of the Examining Committee

_____

Date

Committee in charge:

    Dr. Christopher W. Churchill, Chair

    Dr. Rene A.M. Walterbos

    Dr. Anatoly A. Klypin

    Dr. Michael Engelhardt

DEDICATION

I dedicate this work to my love, Laura, my cat, Stellar, my parents, David & Laurie, and my brother, Gavin.

ACKNOWLEDGMENTS

My greatest thanks to Stellar, for also making sure I wake up each morning by biting my nose. Also for enduring my relentless inane nicknames and providing love and affection in the form of headbutts.

To the European Southern Observatory Science Archive Facility and the Keck Observatory Archive, for organizing and providing access to nearly two decades of observatios.

To Dr. Michael T. Murphy for his aid in collaboration, both providing access to spectacular data and for his detailed input into the science presented in this dissertation.

To Dr. John O'Meara for providing access to yet another spectacular data set.

To Dr. Jane Charlton for collaboration and mentoring well beyond my tenure as her student at Penn State.

To all those who have supported quasar absorption line studies.

To all those who rejected my postdoctoral applications.

EDUCATION

2011-2013   M.S., Astronomy

New Mexico State University

Las Cruces, New Mexico, USA

2007-2011   B.S., Astronomy & Astrophysics

The Pennsylvania State University

State College, Pennsylvania, USA

AWARDS AND GRANTS

2013,2014   New Mexico Space Grant Consortium Graduate Fellowship

2012   Sigma Xi Research Grant

PROFESSIONAL ORGANIZATIONS

American Astronomical Society

PUBLICATIONS

Mathes, N.L., Churchill C.W., and Murphy, M.T., 2017, The Astrophysical Journal, NUMBERS. *The Vulture Survey I: Analyzing the Evolution of MgII Absorbers*

Muzahid, S., Kacprzak, G.G., Churchill, C.W., Charlton, J.C., Nielsen, N.M., Mathes, N.L., and Trujillo-Gomez, S., 2015, The Astrophysical Journal,

811, 132. *An Extreme Metallicity, Large-scale Outflow from a Star-forming Galaxy at z 0.4*

Mathes, N.L., Churchill C.W., Kacprzak, G.G., Nielsen, N.M., Trujilo-Gomez, S., Charlton, J., Muzahid, S., The Astrophysical Journal, 792, 128. *Halo Mass Dependence of H I and O VI Absorption: Evidence for Differential Kinematics*

FIELD OF STUDY

Major Field: Galaxy Evolution
Minor Field: Quasar Absorption Line Spectroscopy

ABSTRACT

The Vulture Survey: Feasting on the Bones of Archival Spectra Left to Die

BY

NIGEL L. MATHES, B.S., M.S.

Doctor of Philosophy

New Mexico State University

Las Cruces, New Mexico, 2012

Dr. Christopher W. Churchill, Chair

We present detailed measurements of the redshift path density, equivalent width distribution, column density distribution, and redshift evolution of Mg II and C IV absorbers as measured in archival spectra from the UVES spectrograph at the Very Large Telescope (VLT/UVES) and the HIRES spectrograph at the Keck Telescope (Keck/HIRES) to equivalent width detection limits below 0.01 Å. This survey examines 432 VLT/UVES spectra from the UVES SQUAD collaboration and 170 Keck/HIRES spectra from the KODIAQ group, representing 580 unique sightlines, allowing for detections of intervening Mg II absorbers spanning redshifts $0.1 < z < 2.6$ and intervening C IV absorbers spanning redshifts $1 < z < 5$. We employ an accurate, automated approach to line detection which consistently detects redshifted absorption doublets. We find that an increased number of high column density Mg II and C IV absorbers at $z = 2$ drives an overall increase in the

quantity of metals around galaxies as compared to the present epoch. We conclude that galaxies eject more metal enriched gas into their halos around $z = 2$ than at any other redshift through star formation driven outflows. We determine that weak Mg II and C IV absorbers, those with equivalent widths less than 0.3 Å, are physically distinct and evolve separately from very strong absorbers, which have equivalent widths greater than 1.0 Å. Over this same time period, evolving ionizing conditions in the halos of galaxies gives rise to an increasing population of low equivalent width, passive Mg II and C IV absorbers. From $z = 2$ to the present, feedback processes decline and we observe fewer very strong systems. From $z = 2$ to $z = 5$, SOMETHING ELSE HAPPENS. EXPLAIN THIS SOMETHING ELSE.

Contents

LIST OF TABLES

LIST OF FIGURES

xiii

LIST OF ABBREVIATIONS

AGN	Active Galactic Nucleus
FITS	Flexible Image Transport System
FWHM	Full-Width Half Max
HIRES	The high-resolution optical spectrograph of the Keck I Telescope
ISM	Interstellar Medium
MW	Milky Way
NASA	National Aeronautics and Space Administration
NSF	National Science Foundation
STScI	Space Telescope Science Institute
UV	Ultraviolet
UVES	The high-resolution optical spectrograph of the VLT
VLT	Very Large Telescope

1. INTRODUCTION

The field of extragalactic astronomy has blossommed in the past decade, with the advent of large telescopes, grand uniform surveys, and the computing power to simulate complex processes on universal scales. By combining observational constraints and cosmological hydrodynamic simulations, we have managed to create galaxies that look like those we have observed for decades. However, as we make more detailed observations revealing the specifics of ever-increasingly complex physical processes, we find that the models do not truly mimic reality. In the end, progress can be made through more detailed observations and more complex simulations.

We know so much more about the material inside galaxies than we do about the material outside galaxies. There exist large reservoirs of gaseous material outside the visible extent of galaxies, in their halos, which must be studied in detail in order to understand how galaxies grow and evolve. In addition, as our understanding of all forms of matter evolves, so must our analysis methods. Individual case studies still have their merit; however, due to the sheer volume of our observable universe and the wild variance in all properties of observable structures, detailed surveys are the next step forward in understanding exactly how our universe works.

This work attempts to begin that process by surveying in great detail the wealth of archived observations at the world's largest, most productive observatories. These data sets make no concessions in resolution or detection sensitivity, and hope to characterize the properties of matter in galaxy halos in great detail so as to trace and predict the full spectrum of gaseous structures throught the

universe.

1.1. Galaxy Formation and Evolution

One of the most elusive yet important goals in extragalactic research aims to discover how galaxies form, grow, and evolve in an effort to truly understand our place in the universe. The creation of a galaxy begins with a cosmic overdensity, where matter congregates to begin the process of building complex structures of stars, gas, and dust. Feedback from star formation and AGN, along with mergers, shape the galaxy and its surroundings into complex environments. The stage of most uncertainty throughout this process involves feedback, the injection of energy into the gaseous medium within and outside of galaxies which, as has been shown in simulations, is required to produce realistic looking galaxies.

The Milky Way serves as the closest and best example of a galaxy. However, galaxies come in all kinds of different shapes and sizes. To truly understand how we came to be, as humans on the planet Earth, we must work to understand how our galaxy came to be, and what processes played part in creating the local environment we live in today.

1.2. The Circumgalactic Medium

Characterizing the baryonic gas processes within and surrounding galaxies is central to understanding their formation and evolution. Quantifying the spatial extent, kinematics, and, in particular, the recycling and/or escape fraction of circumgalactic gas are of primary importance in that they place direct observational constraints on simulations of galaxies and provide insights into the workings of

galaxy evolution.

In general, the gas structures in and around galaxies can be divided into three broad categories: the interstellar medium (ISM), the circumgalactic medium (CGM), and the intergalactic medium (IGM). The CGM, being the gas reservoir that interfaces with the star-forming ISM, outflowing stellar-driven winds, and the accreting IGM, may contain up to 50% of the baryonic mass bound to galaxies (Tumlinson et al. 2011) and account for up to 50% of the baryons unaccounted for in galaxy dark matter halos (Werk et al. 2014). As such, the CGM may play the most critical role in governing the properties of galaxies (e.g., Oppenheimer et al. 2010; Churchill et al. 2013b), including regulatory physics leading to the observed stellar mass function (e.g., **?**) and the stellar mass-ISM metallicity relationship (e.g., Tremonti et al. 2004).

The physical extent of the CGM and the transition zone between the CGM and IGM are currently open questions. Studies by Steidel et al. (2010), Prochaska et al. (2011), and Rudie et al. (2013) indicate a transition from the CGM to the IGM at $\log N(\text{H\,\textsc{i}}) \simeq 14$ and a projected distance of ~ 300 kpc from galaxies at $z \sim 2.5$. At this redshift, $\log N(\text{H\,\textsc{i}}) \simeq 14$ corresponds to an overdensity of $\log \rho_{\text{H}}/\bar{\rho}_{\text{H}} \simeq 0.5$, whereas at $z \simeq 0$, this overdensity would suggest a CGM/IGM transition at $\log N(\text{H\,\textsc{i}}) \simeq 13$ (see Davé et al. 1999). Indeed, Ford et al. (2013) show that, in the over-dense regions hosting galaxies, the extent of the H\,\textsc{i} at fixed column density increases with virial mass, suggesting that a single fiducial physical size for the CGM may not apply across the entire mass range of galaxies; it may be more appropriate to scale CGM properties relative to the virial radius (e.g., **?**Churchill et al. 2013b).

1.3. The Baryon Cycle

One of the most important questions in modern studies of galactic evolution asks, how do baryons cycle into and out of galaxies, and how does this cycle determine the growth and evolution of galaxies themselves? More specifically, how does the process of gas accretion, star formation, and subsequent supernovae-driven feedback shape both the galaxies themselves and their circumgalactic medium (CGM)? By using spectroscopic observations of quasars, we can identify and analyze metal line absorbers in and around the halos of foreground galaxies. Though absorption line studies by themselves cannot directly answer these questions, the statistical results from such studies can provide vital information from which further progress can be made.

1.4. Quasar Absorption Line Spectroscopy

The details of this complex process should be observable in the relationship between the stars in the galaxy and the gas phase material located between the stars within the galaxy (interstellar medium; ISM), just outside the galaxy (circumgalactic medium; CGM), and between galaxies themselves (intergalactic medium; IGM). Unfortunately, detailed observations of this gas are difficult as it remains mostly neutral (CITATION), and therefore does not strongly emit. Therefore, massive efforts have been undertaken to observe this gas in absorption using the most advanced telescopes.

A major problem in studying galaxy evolution at high redshifts is that faint, low mass galaxies cannot be observed with current facilities. These smaller, more numerous galaxies pose major problems when attempting to characterize the ion-

ization conditions of the early universe and detailing the growth history of galaxies. They are all but invisible due to their low luminosities, which makes it nearly impossible to completely inventory galaxy populations and find modern day galaxy analogs at high redshift. Studying properties of galaxy evolution, then, must involve a luminosity-independent tracer of the processes which grow and affect galaxies across cosmic time. One such technique involves observing absorbing gas in quasar spectra, effectively measuring properties of the shadows of gaseous structures around galaxies.

Quasars are exceptionally bright objects, often found at large distances, or high redshift. Their luminosities can exceed SOMETHING BIG, and they can be observed at distances corresponding to light travel times near to that of the beginning of the universe. They serve as extreme cosmic lighthouses, illuminating material located between observers and the quasars themselves.

By taking a spectrum of a quasar, we can learn about material at large distances which may not emit light of its own. By absorbing the light of the quasar at specific wavelengths, this mater, or gas, imprints onto the spectrum a characteristic absorption feature. These absorption features can be measured in order to determine their redshift, and also their underlying physical properties.

1.5.   A Brief History of Mg II Absorption Surveys

One of the most prolific absorption features, the Mg II $\lambda\lambda 2796, 2803$ doublet, traces cool ($T \simeq 10^4$ K; Churchill et al. (2003)) metal enriched gas in the disks and halos of galaxies. It is one of the best tracers of this gas because it can exist in a wide range of ionizing conditions, ranging in ionization parameter from

$-5 < \log U < 1$ (Churchill et al. 1999), it is observable in optical wavelengths for redshifts between $0.1 < z < 2.6$, and it has predictable line characteristics defined by its resonant doublet nature which make it ideal for automated searches.

The origin of Mg II absorbing gas is still debated. As summarized in Kacprzak et al. (2011) and Matejek et al. (2013), two separate interpretations exist to explain the origin of strong, high equivalent width (W_r) Mg II absorbers ($W_r^{\lambda 2796} > 0.3$ Å) and weak, low equivalent width ($W_r^{\lambda 2796} < 0.3$ Å) Mg II absorbers.

For the strong, higher equivalent width systems, multiple correlations exist between the rest frame Mg II equivalent width around galaxies and the host galaxy's star formation properties. Zibetti et al. (2007), Lundgren et al. (2009), Noterdaeme et al. (2010), Bordoloi et al. (2011), and Nestor et al. (2011) all found a correlation betwen $W_r^{\lambda 2796}$ and blue host galaxy color, showing that galaxies with more active star formation have more metal enriched gas in their halos. Bordoloi et al. (2014) also found that Mg II equivalent width increases with increasing star formation rate density. In addition, spectroscopic observations of star forming galaxies have revealed strong Mg II absorption blueshifted $300 - 1000$ km s^{-1} relative to the host galaxy (Tremonti et al. 2007; Weiner et al. 2009; Martin & Bouché 2009; Rubin et al. 2010).

Multple correlations have also been found between the equivalent width of strong Mg II absorbers and host galaxy mass. Bouché et al. (2006) found an anti-correlation between galaxy halo mass, derived from the cross-correlation between Mg II absorption systems and luminous red galaxies, and Mg II equivalent width, showing that individual clouds of a Mg II system are not virialized in the halos of galaxies. They interpreted their results as a strong indication that high equivalent

width absorbers with $W_r^{\lambda 2796} \gtrsim 2$ Å arise in galactic outflows. Marginal anti-correlations between Mg II equivalent width and galaxy halo mass using the same cross-correlation method were also reported by Gauthier et al. (2009) and Lundgren et al. (2009). It is imporant to note, however, that Churchill et al. (2013a) and Churchill et al. (2013b) find no correlation between $W_r^{\lambda 2796}$ and halo mass when halo mass is derived from abundance matching. They instead find that galaxies inhabiting more massive dark matter halos have stronger absorption at a given distance.

For the weak, lower equivalent width systems, it seems none of the above correlations hold. Chen et al. (2010), Kacprzak et al. (2011), and Lovegrove & Simcoe (2011) found little evidence for a correlation between galaxy color and Mg II equivalent width when restricting their samples to weak absorbers. Kacprzak et al. (2011) measured the orientation of galaxies relative to Mg II detections in the sight lines of background quasars and identified low metallicity, low equivalent width Mg II absorbers co-planar with some some galaxy disks, implying structures associated with accreting filaments as opposed to outflows, which are more often observed perpendicular to the galaxy disk (Bordoloi et al. 2011; Kacprzak et al. 2012; Bouché et al. 2012). Finally, the simulations of Stewart et al. (2011) and Ford et al. (2013) revealed a reservoir of low-ionization, metal enriched, co-rotating gas around massive galaxies. Together, these studies imply that weak Mg II absorption systems may preferentially trace low metallicity infall and co-rotating gas in the circumgalactic medium.

Nielsen et al. (2013b) constructed a sample of Mg II absorbers and their associated galaxies and examined both strong and weak Mg II absorbers from $0.07 \leq z \leq 1.1$. In the subsequent analysis of their sample, Nielsen et al. (2013a)

found a more extended Mg II absorbing CGM around higher luminosity, bluer, higher redshift galaxies. In addition, in Nielsen et al. (2016), they found that bluer galaxies replenish their Mg II absorbing CGM through outflows, whereas red galaxies do not. Finally, in Nielsen et al. (2015), it is made clear that the largest velocity dispersions in Mg II absorbing systems are measured around blue, face-on galaxies probed along their minor axis, strongly suggesting that these Mg II absorbers originate in bi-conical outflows.

Many surveys have been undertaken to inventory Mg II absorbers and examine their evolution. The earliest studies (Lanzetta et al. 1987; Tytler et al. 1987; Sargent et al. 1988; Steidel & Sargent 1992) found that Mg II systems with rest equivalent widths above 0.3 Å show no evolution in $d\mathcal{N}/dz$ between redshifts $0.2 < z < 2.15$. These studies also found that the equivalent width distribution function, $f(W_r^{\lambda 2796})$, could be fit equally well with either an exponential or a power-law function. It remains uncertain whether the cosmic distribution of Mg II in galactic halos exhibits a fractal, self-similar nature, or if $f(W_r^{\lambda 2796})$ flattens at equivalent widths below $W_r^{\lambda 2796} < 0.3$ Å.

Mg II absorption surveys have taken one of two different approaches to try to analyze the global distribution of Mg II absorbing gas across cosmic time. Churchill et al. (1999) and Narayanan et al. (2007) aimed to determine more precisely how $d\mathcal{N}/dz$ and $f(W_r^{\lambda 2796})$ evolve with redshift by surveying weak Mg II absorbers. They found that, for these low equivalent width absorbers, $d\mathcal{N}/dz$ increases as a function of increasing redshift up until $z = 1.4$. At higher redshifts, $d\mathcal{N}/dz$ falls to lower values, though the uncertainties are large. In addition, they found the equivalent width distribution function for weak absorbers is best fit by a power-law, strongly disfavoring an exponential fit to the overall distribution.

The most recent studies have employed new multi-object spectrographs such as the Sloan Digital Sky Survey (SDSS) and the FIRE spectrograph on the Magellan Baade Telescope (Nestor et al. 2005; Matejek & Simcoe 2012; Chen et al. 2016). Nestor et al. (2005), who examined over 1300 intervening Mg II absorbers in SDSS quasar spectra with $W_r^{\lambda 2796} > 0.3$ Å, found that the equivalent width distribution function is well fit by an exponential. They did not find evidence for redshift evolution in systems with $0.4 < W_r^{\lambda 2796} < 2$ Å, but observed an enhancement in the number of $W_r^{\lambda 2796} > 2$ Å absorbers per comoving redshift path length as a function of increasing redshift from $z \sim 0$ up to $z \sim 2$. Matejek & Simcoe (2012) and Chen et al. (2016), analyzing 279 Mg II absorbing systems from $2 < z < 7$ in infrared FIRE spectra, also found that the equivalent width distribution function is well fit by an exponential. They also observed that systems with $W_r^{\lambda 2796} < 1.0$ Å show no evolution with redshift, but higher equivalent width systems grow in number density from low redshift to $z \sim 3$, after which the number density declines. Collectively, these surveys imply physical changes in the astrophysical processes or in the state of the gas structures in the environments giving rise to Mg II absorption as the universe ages.

1.6. A Brief History of C IV Absorption Surveys

The first study to characterize the distribution of intervening CIV absorbers was /citeYoung1982, which determined that these lines were randomly distributed in redshift in a manner consistent with absorption from intervening galaxies. /citeSargent1988 also showed that the number density of systems per unit redshift decreases with increasing redshift from $1.8/lez_{em}/le3.56$. /citeSteidel1990, examining strong CIV absorbers at redshifts between $1.3/lez_{abs}/le4.0$, found also that

the number of CIV absorption systems per unit redshift range decreases with increasing redshift, in a manner inconsistent with a constant comoving density of absorbers. Therefore, they stated, the properties of CIV absorbers must evolve over time.

In terms of kinematics, /citeSteidel1990 noted that the peak in the CIV two-point correlation function on velocity scales $200/le\Delta v/le600$ km s^{-1} appears to have the same power at low and high redshift. /citeRauch1996 examined the velocity structure of intervening CIV absorbers in the spectra of 3 intermediate redshift quasars and detrmined that gas temperatures were likely near $3.8/times10^4$ /mathrmk, and the TPCF of CIV systems suggests that there is more than one source of velocity dispersion. They interpret the shape of the resulting TPCF as owing to ensembles of objects with the kinematics of dwarf galaxies on a small scale, while following the Hubble flow on a larger scale.

Churchill et al. (1999) examined data from the Hubble Space Telescope Faint Object Spectrograph for CIV absorbers associated with known MgII absorbers measured in high resolution Keck/HIRES data. They noticed a strong correlation between MgII kinematics and CIV equivalent width. They interpreted that this correlation could imply a connection between outflowing MgII clouds and higher ionization state halo gas.

Rauch et al. (2001) measured the kinematics and column density differences of CIV absorption systems along the lines of sight to three gravitationally lensed quasars. They found the spatial distribution of the gas to be mostly featureless with detectable velocity shear up to $\sim$ 70 kms. They found the clouds quiescent, in that the energy transmitted to the gas as measured by the amount of turbu-

lence derived along the line of sight, and therefore determined that the absorbing structures are not internal to galaxies. They posited that C IV absorbers could be gas expelled recently or pre-enriched from earlier star formation.

Chen et al. (2001) examined 14 galaxy absorber pairs, along with 36 galaxies without associated C IV absorption lines. They found that C IV absorption line systems cluster strongly on velocity scales of $v \lesssim 250$ km s^{-1} and impact parameter scales of $\rho \lesssim 100$ h^{-1} kpc. In addition, they note that galaxies of all morphological types and luminosities can possess extended gaseous envelopes, with covering factors near unity, at impact parameters less than 100 kpc. They concluded that accreting satellites are the most likely sources of this metal enriched halo gas.

Simcoe et al. (2004) directly measured the metallicity distribution function for the $z \sim 2.5$ intergalactic medium in the spectra of seven quasars. They found no evidence for a universal metallicity floor, as had been suggested for some scenarios of Population III enrichment in the early universe. In addition, they found no trends in metallicity as a function of IGM density.

Fox et al. (2007) studied 63 damped Lyman-α (DLA) systems and 11 sub-DLAs with associated C IV absorption. They detected C IV clouds moving at velocites in excess of the escape speed, determined by measuring the total line width of the neutral gas profile, in roughly 40% of their systems. They inferred that these clouds may arise in high ionized outflowing winds, powered by galaxies with star formation rates (SFR) of ~ 2 $M_\odot$ yr^{-1}.

Shull et al. (2014) used *HST*/COS spectra of background quasars to measure elemental abundances in the low redshift intergalactic medium. They found that C IV has increased in abundance by a factor of 10 from $z \sim 5$ to present.

Bordoloi et al. (2014) measured C IV absorption in the COS-Dwarfs survey, probing the gaseous halos near 43 low-mass galaxies at $z \geq 0.1$. They detected C IV out to ~ 100 kpc, roughly $0.5 R_{vir}$, from the host galaxies. They also reported a tentative correlation between C IV equivalent width and SFR, and concluded that energy-driven star formation winds must expel into the CGM a comparable mass to that of the carbon found in the stars of these galaxies.

1.7. Project Goals

The goal of this project is to wrest my PhD from the icy grips of my faculty captors.

2. DATA

2.1. Spectral Properties

Properties of UVES and HIRES and things.

Table of spectroscopic observations of quasars.

2.2. Reduction and Pre-Analysis

Describe reduction process for each instrument and describe the processes of higher order continuum fitting and things like that.

2.3. Redshift Path Length

Describe g of w z and show the pretty heat map plot and explain it.

3. AUTOMATED LINE DETECTION

3.1. Motivating Automated Line Detection

Large spectral data sets are becomming the norm in both galactic and extragalactic astronomy. In the Milky Way, the spectra of hundreds of thousands of stars may be analyzed by routines which fit templates to find the best agreement. Unfortunately, when dealing with redshifted systems composed of a multitude of components (stars, gas, AGN), the number of free parameters increases significantly and templates/matching techniques become unfeasable. Therefore, we require a more general, but no less robust line finding algorithm to handle large spectral libraries.

3.2. Defining the Search Window

In any large survey, a well-defined search window is important. In the case of analyzing quasar spectra, we are constrained by several factors: the wavelength coverage of the spectrum, the redshift of the observed quasar, and the confidence with which we can identify individual doublets in regions of low signal-to-noise and regions with atmospheric absorption features (telluric lines).

We first limit the search range to regions of the spectrum redward of the Ly α emission, as Ly α forest contamination would render automatic detection of weaker metal lines nearly impossible. We also do not search 5000 km s^{-1} blueward of the quasar emission redshift in order to avoid absorbers associated with the quasar itself. Finally, we exclude regions of strong telluric absorption bands, specifically from $6277 - 6318$ Å, $6868 - 6932$ Å, $7594 - 7700$ Å, and $9300 - 9630$ Å, because we found that the molecular line separations and ratios can lead to numerous false

positives when searching for Mg II doublets.

3.3. Matched Filtering Algorithm

We employ a matched filter search method similar to that of Zhu & Menard, 2013, seeking line candidates above a certain signal-to-noise ratio threshold. This process involves correlating a template filter (in this case, a tophat function) with a signal to detect the presence of features matching the template. In other words, we convolve the quasar spectrum with a conjugated, reversed filter representing an absorption trough. This method can maximize the signal-to-noise ratio in the presense of stochastic noise.

The filter we choose is a top hat function centered at the wavelength of the desired redshifted absorption line. Its width is selected to match the resolution of the spectrum, which is a function of the slit width used during the exposure. A large variety of slit-widths were used to achieve different resolutions for varying science drivers, but, characteristically for a 1.0 arcsec slit, $R \sim 40,000$ for VLT/UVES and $R \sim 45,000$ for Keck/HIRES. We convolve the filter with the normalized spectrum to generate a normalized power spectrum in redshift space, with absorption features having positive power.

The error spectrum in both instruments is complex, irregular, and has frequent single-pixel spikes which makes uniform normalization impossible. Therefore, we cannot convolve the filter with the error spectrum to derive normalized noise estimates, as is often done in matched filter analysis. Instead, we examine the noise in the derived power spectrum.

To derive the noise, we first divide the power spectrum into smaller chunks

which correspond to roughly 3000 pixels in the observed spectrum. We then sigma-clip these chunks to remove absorption features, leaving only the continuum power spectrum. Next, we calculate the standard deviation of this continuum. Finally, we use the standard deviation as the noise to calculate the S/N of the absorption features in the power spectrum as the ratio of the normalized power (S) to the normalized noise (N).

A flagged absorption feature has $S/N > 5$. A confirmed doublet detetection for Mg II $\lambda\lambda 2796, 2803$ requires detection of $S/N^{\lambda 2796} > 5$ and $S/N^{\lambda 2803} > 3$. Similarly, a detection for C IV $\lambda\lambda 1548, 1550$, we require $S/N^{\lambda 1548} > 5$ and $S/N^{\lambda 1551} > 3$. In addition, our automated routines remove detections with non-physical doublet ratios in unsaturated regions; specifically, we exclude cases where $W_r^{\lambda 2803} > W_r^{\lambda 2796}$, or $W_r^{\lambda 2803} < \left(0.3 \times W_r^{\lambda 2796}\right)$. The same convention is also applied to the C IV doublets. The latter constraint is conservative for unsaturated absorbers, as the secondary transition in the doublet is rarely observed less than $0.5\times$ the primary. We relax this constraint in saturated features. This system could potentially exclude detections where either the primary or secondary line in the doublet is blended with another transition but does not saturate; however, confirmation of these cases requires extra verification from separate ionic transitions, such as Fe II, which are weaker and not always covered in the spectrum.

All absorption features are visually verified upon completion of the detection algorithm. Multiple feature detections within ± 500 km s^{-1} of each other are grouped together to generate absorption systems, designated as a single absorber, to be analyzed. Once absorption systems are identified, we calculate the optical depth-weighted median absorption redshift to define the center of the entire absorption system. The formal derivation of this redshift is described in the

16

appendix of **?**.

We also derive an equivalent width detection limit across the spectrum. To do so, we insert modelled Gaussian absorption features across the spectrum and assume a full-width at half maximum (FWHM) defined by the resolution of the instrument to represent unresolved lines. We then solve for the height of the Gaussian, defined as the value at the curve's peak, required to detect the unresolved line with our matched filtering technique at a $S/N = 5$. Finally, we integrate to find the equivalent width, and take that value as the minimum detectable equivalent width at a given wavelength. The detection algorithm is therefore self-monitoring. This full equivalent width detection limit spectrum also allows us to accurately characterize the completeness of our sample, along with the full redshift path length searched.

3.4.   The Step-By-Step Recipe for Finding Redshifted Lines

1. Define Search Window

2. Convert wavelength search window to a redshift range for each ion to search

3. Define redshift resolution based upon the spectrograph resolution

4. Define filter sized based upon FWHM of an unresolved line at the given spectrograph resolution

5. Do the cross-correlation

   - At each redshift, place the filter for each transition (Mg II $\lambda\lambda 2796, 2803$ and C IV $\lambda\lambda 1548, 1550$).

- Compute the area between the filter and the observed spectrum - This is the power at that redshift. Higher power corresponds to stronger absorption.

- Step forward, repeat the calculation. Build up a power spectrum which has the observed power for each transition at a given redshift.

6. Normalize the power spectrum.

- The raw power spectrum's amplitude is tied directly to the wavelength range (or redshift range depending on how you want to think about it at this point), as we are taking the area beneath a variable-length object (in this case, the spectrum or filter). We wish to analyze a power spectrum which ranges between 0 and 1 for any spectrum analyzed. This means we want to subtract the baseline value (the result of the correlation if there is zero absorption detected) from the raw power spectrum, and then divide by the difference between the minimum value (no absorption) and the maximum value (a fully saturated absorption line whose width is equal to or greater than the width of the filter used).

- This difference ends up being the area of the filter, which, because the spectrum is normalized, is the width of the filter.

7. Calculate the normalized error.

- Split the normalized power spectrum into chunks (HOW BIG ARE THEY).

- In each of these chunks, sigma clip the power spectrum to eliminate

absorption features.

- Take the standard deviation of the remaining power spectrum. This represents the noise in the continuum after filtering.

4.   ANALYSIS OF ABSORPTION PROPERTIES

This is how we look at squiggles and tell you they mean something.

4.1.   Equivalent Width Regions

We put windows on things.

4.2.   Calculating Redshifts and Velocities

Something something optical depth weighted medians.

4.3.   Equivalent Widths and Kinematic Spreads

Integrate the things and do something with tau.

4.4.   Column Densities

AOD stuff here.

5.   PROPERTIES AND EVOLUTION OF MGII ABSORBERS

Now we can finally get down to the science!

5.1.   Number of Absorbers Per Path Length

The largest sample of quasar spectra originates from the Sloan Digital Sky Survey (SDSS), with more than 10^5 spectra at present, which employs a spectrograph with an instrumental resolution around 69 km s^{-1}, limiting SDSS absorption surveys to strong absorbers, with $W_r^{\lambda 2796} \geq 0.3$ Å (Nestor et al. 2005; ?). Conversely, previous studies of weak absorbers used small samples of quasar spectra, never exceeding 100 quasar spectra (Steidel & Sargent 1992; Narayanan et al. 2007; Kacprzak et al. 2011). In this paper, we aim to characterize the evolution of the incidence rate, number of absorbers per redshift path length, comoving line density, and cosmic mass density of all MgII absorbers from redshifts $0.18 < z < 2.57$.

The number of MgII absorbers per redshift path length and its associated variance are defined as

$$\frac{d\mathcal{N}}{dz} = \sum_i \frac{1}{\Delta Z_i\,(W_r)}, \quad \sigma^2_{\frac{d\mathcal{N}}{dz}} = \sum_i \left[\frac{1}{\Delta Z_i\,(W_r)}\right]^2, \tag{5.1}$$

where we count the number of MgII absorbers, dividing by the total searched redshift path length (ΔZ), defined as

$$\Delta Z_i\,(W_r) = \int_{z_1}^{z_2} g_i\,(W_r, z)\,dz, \tag{5.2}$$

21

where $g_i(W_r, z)$ is the equivalent width sensitivity function at a given equivalent width detection limit shown in Equation **??**. The function $g(W_r, z)$, first formulated in Lanzetta et al. (1987), details the number of spectra in which an absorption feature with a given equivalent width may be detected at the 5σ level in a given redshift interval.

The comoving Mg II line density and its associated variance are defined as

$$\frac{d\mathcal{N}}{dX} = \sum_i \frac{1}{\Delta X_i (W_r)}, \quad \sigma^2_{\frac{d\mathcal{N}}{dX}} = \sum_i \left[\frac{1}{\Delta X_i (W_r)} \right]^2, \qquad (5.3)$$

where we count the number of Mg II absorbers, dividing by the total searched absorption path (ΔX), defined as

$$\Delta X_i (W_r) = \int_{z_1}^{z_2} g_i (W_r, z) \frac{(1+z)^2}{\sqrt{\Omega_M (1+z)^3 + \Omega_\Lambda}} \, dz, \qquad (5.4)$$

where Ω_M is the cosmic matter density, and Ω_Λ is the cosmic density attributed to dark energy. Counting with respect to ΔX accounts for both cosmological expansion along the line of sight and the transverse separation of objects with unchanging number density and cross section, allowing for more consistent comparisons across redshift.

In Figure 5.1, we plot $d\mathcal{N}/dz$ and $d\mathcal{N}/dX$, respectively, as a function of redshift for different minimum equivalent width thresholds, such that detected Mg II absorbers have equivalent widths greater than $W_{r,\mathrm{min}}^{\lambda 2796}$. Error bars in each bin represent 1σ uncertainties calculated according to Equations 5.1 and 5.3. Dotted lines are fit according to the analytical form which allows for redshift evolution in $d\mathcal{N}/dX$, defined as,
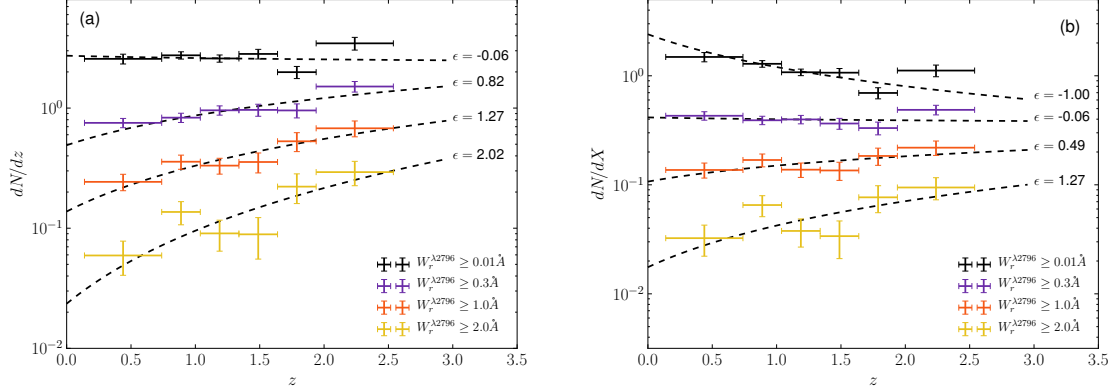
Fig. 5.1.— (a) $d\mathcal{N}/dz$ and (b) $d\mathcal{N}/dX$ as a function of redshift for different minimum equivalent width thresholds, $W_{r,\mathrm{min}}^{\lambda 2796}$. Colors represent different $W_{r,\mathrm{min}}^{\lambda 2796}$. The black dotted lines are fits to the distribution of the functional form $f(z) = \frac{c}{H_o} n_0 \sigma_0 (1+z)^{\epsilon}$, with the best fit ϵ value labelled. We see increasing values of ϵ with increasing equivalent width, driven by an enhancement of stronger Mg II absorbers around redshift 2 compared to lower redshifts. Vertical error bars represent 1σ uncertainties in each bin.

$$\frac{d\mathcal{N}}{dX}(z) \equiv \frac{c}{H_o} n(z)\, \sigma(z) = \frac{c}{H_o} n_0\, \sigma_0\, (1+z)^{\epsilon}, \qquad (5.5)$$

where c is the speed of light, H_o is the Hubble Constant, n_0 is the comoving number density of Mg II absorbers at $z = 0$, σ_0 is the absorbing cross-section at $z = 0$, and ϵ is the evolution parameter, defined as the power dependence of $d\mathcal{N}/dX$ on redshift. We fit to the binned data using an orthogonal distance regression (ODR) method implemented in Python[1]. We use this approach in all cases where functional fits are applied, and discuss the robustness of this method in Section ??.

The product $n_0\,\sigma_0$ represents a comoving opacity of Mg II-selected absorption line systems by virtue of the units, which are an inverse length, and the analogous

---

[1]https://docs.scipy.org/doc/scipy/reference/odr.html

23

absorption coefficient to describe the opacity of material in stellar atmospheres. The full product of $\frac{c}{H_o} n_0 \sigma_0$ then represents the Hubble optical depth for MgII absorbers. We find that the best-fit value of ϵ is negative when analyzing the full sample of MgII absorbers, including all detections with measured equivalent widths above $W_r^{\lambda 2796} > 0.01$ Å. The evolution parameter, ϵ, then increases with subsequently larger minimum equivalent width thresholds, becoming positive for absorbers with $W_{r,\mathrm{min}}^{\lambda 2796} > 1.0$ Å. This trend is driven primarily by an enhancement in $d\mathcal{N}/dX$ for the strongest MgII absorbers around $z \sim 2$, relative to lower redshifts. Conversely, at low redshift we observe more weak MgII absorbers per absorption path length. We show in Table 5.1 the values of the fit parameters for varying $W_{r,\mathrm{min}}^{\lambda 2796}$, along with their 1σ uncertainties.

In Figure 5.2, we show the values of $\frac{c}{H_o} n_0 \sigma_0$ and ϵ as a function of $W_{r,\mathrm{min}}^{\lambda 2796}$. The shaded red areas represent the 1σ standard deviations derived from the fits to the $d\mathcal{N}/dX$ distribution. We show first that the comoving Hubble optical depth of MgII absorbers decreases as a function of $W_r^{\lambda 2796}$. This implies that, per unit absorption path length, there are fewer high equivalent width MgII absorbers, and/or that they exist in smaller absorbing structures. We also show that the

Table 5.1. Parameterization of $d\mathcal{N}/dX$

$W_{r,\mathrm{min}}^{2796}$ [Å]	$\frac{c}{H_o} n_0 \sigma_0$	ϵ
0.01	2.583 ± 0.827	-1.04 ± 0.38
0.30	0.446 ± 0.076	-0.14 ± 0.21
1.00	0.116 ± 0.043	0.31 ± 0.44
2.00	0.019 ± 0.014	0.94 ± 0.85

24
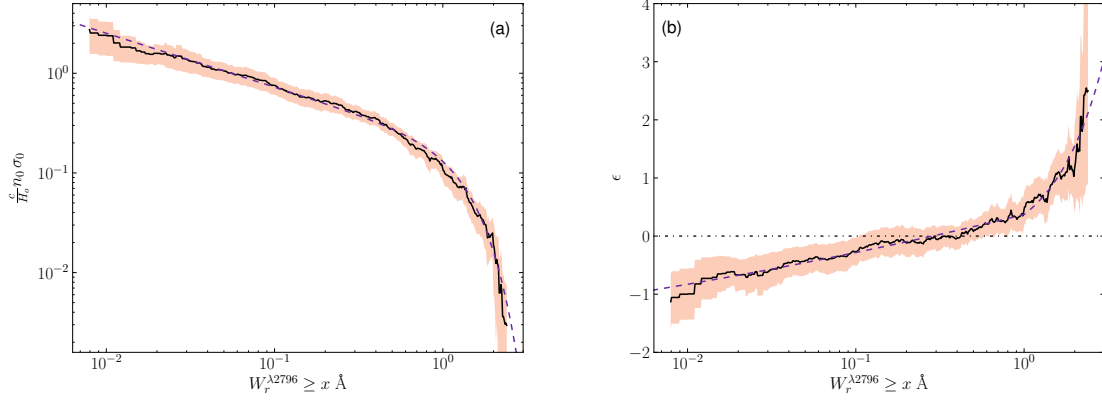
Fig. 5.2.— (a) The comoving number density of absorbers multiplied by the absorbing cross-section, derived by fitting Equation 6.1 to $d\mathcal{N}/dX$, as a function of $W_{r,\text{min}}^{\lambda 2796}$ with shaded 1σ uncertainties. As we examine samples with increasing minimum Mg II equivalent width thresholds, either the space density of absorbing cloud structures decreases, the absorbing cross-section decreases, or both parameters decrease. (b) The redshift evolution parameter, ϵ, as a function of $W_{r,\text{min}}^{\lambda 2796}$. Weak Mg II absorbers are more abundant at low redshift, leading to a negative coefficient ϵ. Absorbers with equivalent widths near 0.3 Å do not evolve, with $\epsilon \simeq 0$. Strong Mg II absorbers evolve away at low redshift, showing a large positive ϵ increasing towards $z \sim 2$.

slope of the redshift dependence, ϵ, increases as a function of increasing $W_{r,\text{min}}^{\lambda 2796}$. This evolution parameter, ϵ, changes from negative to positive toward higher equivalent width Mg II absorbers, implying that strong Mg II absorbers evolve away, decreasing in relative number per absorption path length, from $z = 2$ to present. Conversely, weak Mg II absorbers build up over time, increasing in relative number per absorption path length from $z = 2$ to present. We observe no evolution with redshift in absorbers with equivalent widths between $0.3 < W_r^{\lambda 2796} < 1$ Å.

We provide a parameterized fit to $\frac{c}{H_o} n_0 \sigma_0$ and ϵ as a function of $W_{r,\text{min}}^{\lambda 2796}$. In Figure 5.2(a), we adopt a power-law with a generalized exponential decay to model the $\frac{c}{H_o} n_0 \sigma_0$ distribution, defined as,

$$\frac{c}{H_o} n_0 \, \sigma_0 \, (\, \psi \,) = \Psi^* (\, \psi \,)^{\alpha} e^{-\psi^{\beta}}, \tag{5.6}$$

where $\psi = W_{r,\mathrm{min}}^{\lambda 2796}/W_{r,\mathrm{min}}^*$ to simplify the equation. The best fit parameters are $\Psi^* = 0.24 \pm 0.01$, $W_{r,\mathrm{min}}^* = 1.19 \pm 0.02$, $\alpha = -0.49 \pm 0.01$, and $\beta = 1.50 \pm 0.05$. This parameterization resembles a Schechter function, but we required an exponential drop-off at the high end faster than $e^{-\psi}$, which manifests itself in the form of β. Next, in Figure 5.2(b), we fit a broken power-law to the ϵ distribution, defined as,

$$\epsilon\,(W_{r,\mathrm{min}}^{\lambda 2796}) = \begin{cases} a_1 \, (\, W_{r,\mathrm{min}}^{\lambda 2796} \,)^{\gamma_1} + b_1 & \text{if } \ W_{r,\mathrm{min}}^{\lambda 2796} < 1.1 \ \mathring{\text{A}} \\[2mm] a_2 \, (\, W_{r,\mathrm{min}}^{\lambda 2796} \,)^{\gamma_2} + b_2 & \text{if } \ W_{r,\mathrm{min}}^{\lambda 2796} \geq 1.1 \ \mathring{\text{A}}, \end{cases} \tag{5.7}$$

where the fit parameters for minimum equivalent width thresholds below 1.1 Å are $a_1 = 3.13 \pm 1.49$, $\gamma_1 = 0.09 \pm 0.05$, and $b_1 = 2.87 \pm 1.49$. The fit parameters for the power-law with $W_{r,\mathrm{min}}^{\lambda 2796} \geq 1.1$ Å are $a_2 = 0.07 \pm 0.01$, $\gamma_2 = 3.73 \pm 0.25$, and $b_2 = -0.21 \pm 0.03$. Combining the fits to $\frac{c}{H_o} n_0 \, \sigma_0$ and ϵ, we now have an analytic parameterization of $d\mathcal{N}/dX$ as a function of $W_{r,\mathrm{min}}^{\lambda 2796}$, and z, of the form,

$$\frac{d\mathcal{N}}{dX}(W_{r,\mathrm{min}}^{\lambda 2796}, z) = \Psi^* \psi^{\alpha} e^{-\psi^{\beta}} (1+z)^{\epsilon(W_{r,\mathrm{min}}^{\lambda 2796})}. \tag{5.8}$$

This function can be used in future semi-analytic models to parameterize the physical properties of Mg II absorbers in galaxy halos (e.g. ?).

5.2. Equivalent Width Distribution

To calculate the equivalent width frequency distribution $f(W)$, the number of absorbers of a given equivalent width per unit path density, we calculate $d\mathcal{N}/dz$

or $d\mathcal{N}/dX$ for each equivalent width bin and divide by the bin width. We split the sample into four redshift regimes, ensuring that the number of absorbers in each redshift subsample remains constant. The result is a characteristic number of MgII absorbers per redshift or absorption path length per equivalent width.

Fig. 5.3.— (a) The equivalent width distribution of MgII absorbers, defined as the redshift path density $(d\mathcal{N}/dz)$ in each equivalent width bin divided by the bin width. (b) The equivalent width distribution, defined as the comoving line density $(d\mathcal{N}/dX)$ in each equivalent width bin divided by the bin width. Error bars represent 1σ uncertainties in each bin. We fit each distribution with a Schechter function, capturing the self-similar power-law behavior of weak MgII absorbers and the exponential power-law cutoff when observing the strongest MgII systems.

In Figure 5.3, we plot the equivalent width frequency distribution with respect to either $d\mathcal{N}/dz$ or $d\mathcal{N}/dX$. We fit each distribution with a Schechter function of the form,

$$\Phi(W_r) = \Phi^* \left(\frac{W_r}{W_r^*}\right)^\alpha e^{-W_r/W_r^*}, \tag{5.9}$$

where Φ^* is the normalization, α is the low equivalent width power-law slope, and W_r^* is the turnover point in the distribution where the low equivalent width power-

law slope transitions into an exponential cutoff. Table 5.2 shows the values of Φ^*, W_r^*, and α, along with their associated 1σ uncertainties derived from the fitting routine. This functional fit is motivated by papers such as **?**, where the authors seek to combine previous surveys of strong Mg II absorbers, in which exponential fits were preferred, and surveys of weak Mg II absorbers, where power-laws best fit the equivalent width distribution. The power-law nature of the distribution of weak absorbers in our survey is apparent, and the exponential cutoff is motivated by physical limits to the size, density, and velocity widths of Mg II absorbing clouds. Examining the distribution as a function of redshift, we find the low equivalent width slope becomes more shallow at $z \sim 2$ compared with the present epoch, with $\alpha = -1.09$ in our subsample with $0.14 \leq z < 0.78$ and $\alpha = -0.81$ in our subsample with $1.53 < z \leq 2.64$. We observe fewer weak Mg II absorbers and more strong Mg II absorbers per redshift/comoving absorption path length at $z \sim 2$ than we do at $z \sim 0.5$.

Table 5.2. Schechter Fit to $f(W) = \frac{d\mathcal{N}}{dX}/\Delta W$

Redshift Range	Φ^*	W^* [Å]	α
$0.14 - 0.78$	0.15 ± 0.10	1.72 ± 0.68	-1.09 ± 0.09
$0.78 - 1.09$	0.12 ± 0.06	2.36 ± 0.81	-0.99 ± 0.06
$1.09 - 1.53$	0.11 ± 0.03	2.00 ± 0.35	-1.02 ± 0.04
$1.53 - 2.64$	0.12 ± 0.08	2.25 ± 0.87	-0.81 ± 0.12

5.3.   Column Density Distribution

To calculate the column density distribution, the number of absorbers of a given column density per unit path density, we calculate $d\mathcal{N}/dz$ or $d\mathcal{N}/dX$ for each column density bin and divide by the bin width. The result is a characteristic number density of Mg II absorbers per redshift or absorption path length as a function of their column densities. It should be noted that at high column densities near $\log(N(\mathrm{Mg\,II})) = 15$ cm^{-2}, the measured column densities are lower limits as the AOD method cannot constrain the true column when the absorption line becomes saturated. In these cases, we turn to the Mg II $\lambda 2803$ profile, adopting its value of column density instead.
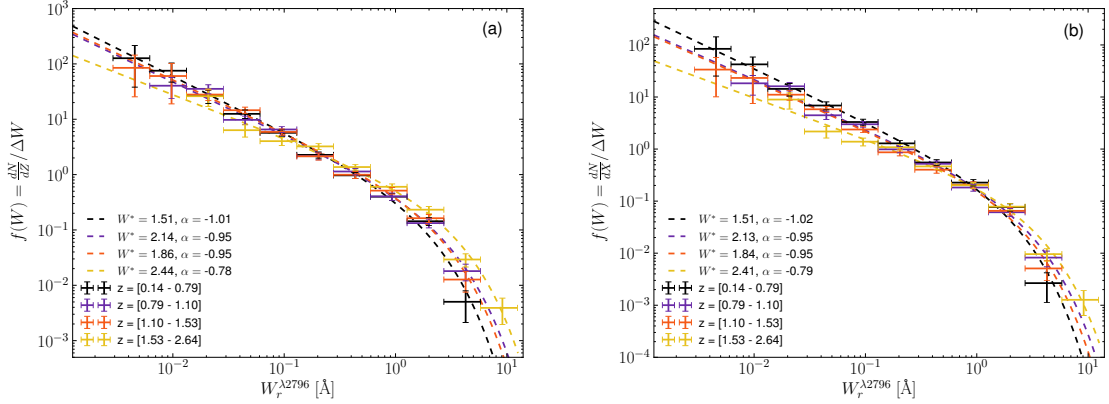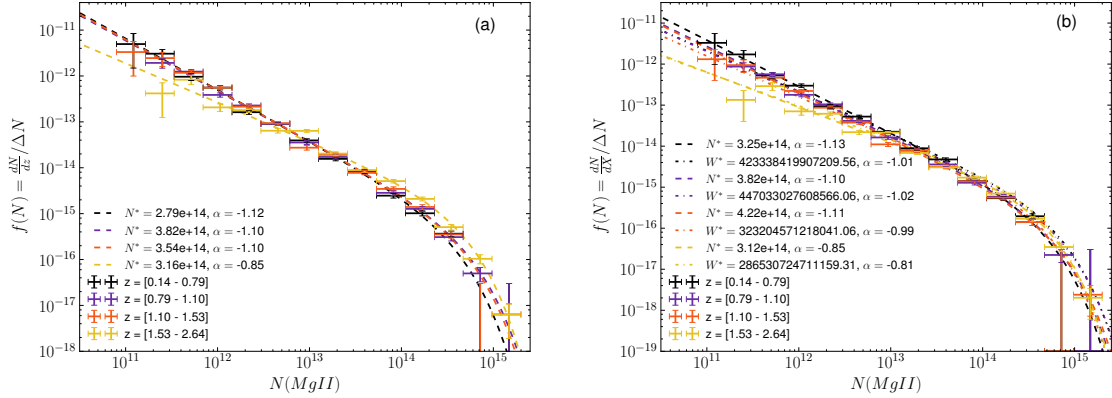

Fig. 5.4.— (a) The column density distribution of Mg II absorbers, defined as the redshift path density $(d\mathcal{N}/dz)$ in each column density bin divididded by the bin width. (b) The comoving line density $(d\mathcal{N}/dX)$ in each column density bin divided by the bin width. We fit this distribution with a Schechter function to accurately parameterize the low column density power-law slope and the exponential cutoff and high column densities.

In Figure 6.8, we plot the column density frequency distribution using either $d\mathcal{N}/dz$ or $d\mathcal{N}/dX$. Again, we fit this distribution with a Schechter function of the

same form as Equation 5.9, except with equivalent width replaced with column density. Table 5.3 shows the values of Φ^*, N^*, and α, along with their associated 1σ uncertainties. We find again that the low column density slope is shallower near $z \sim 2$ than at $z \sim 0.5$. Due to saturation effects, the highest column density measurements may still be lower limits based upon the Mg II $\lambda2803$ profile; therefore, the final high column density bin in $f(N)$ may be regarded as an upper limit. These limits are taken into account in the functional fitting procedures, where using the ODR fitting method we inflate the uncertainties in the positive x and y directions commensurate with the number of limit measurements.

5.4. $\Omega_{\mathrm{Mg\,II}}$

We now aim to calculate the matter density of Mg II absorbers across cosmic time. To do so, we employ the following customary equation relating the mass density of an ion as a fraction of the critical density today to the first moment of the column density distribution,

Table 5.3.   Schechter Fit to $f(N) = \frac{d\mathcal{N}}{dX}/\Delta N$

Redshift Range	Φ^* $[\times10^{-16}]$	N^* $[\times10^{14}\ \mathrm{cm}^{-2}]$	α
$0.14 - 0.78$	8.79 ± 8.19	1.71 ± 0.97	-1.14 ± 0.08
$0.78 - 1.09$	6.41 ± 2.43	2.29 ± 0.56	-1.10 ± 0.03
$1.09 - 1.53$	4.15 ± 2.40	2.65 ± 1.00	-1.12 ± 0.04
$1.53 - 2.64$	7.98 ± 6.51	2.35 ± 1.32	-0.91 ± 0.08

$$\Omega_{\mathrm{Mg\,II}} = \frac{H_0 \; m_{\mathrm{Mg\,II}}}{c \; \rho_{c,0}} \int_{N_{min}}^{N_{max}} f(N_{\mathrm{Mg\,II}}) \, N_{\mathrm{Mg\,II}} \, dN_{\mathrm{Mg\,II}}, \qquad (5.10)$$

where H_0 is the Hubble constant today, $m_{\mathrm{Mg}} = 4.035 \times 10^{-23}$ g, c is the speed of light, $\rho_{c,0}$ is the critical density at present, $f(N_{\mathrm{Mg\,II}})$ is the column density distribution of Mg II absorbers, and $N_{\mathrm{Mg\,II}}$ is the column density. Using our derived fit to the column density distribution, we are able to numerically integrate the first moment from $0 < \log N(\mathrm{Mg\,II}) < 20$ cm^{-2}. The upper limit of $\log N(\mathrm{Mg\,II}) < 20$ cm^{-2} is chosen as an effective infinity, where upper integration limits above this value produced no discernable differences in the calculation. Limiting the integral in this manner did nothing more than shorten calculation times when deriving errors, as described below.

The results are shown below in Figure 6.9. 1σ uncertainties are derived with a bootstrap Monte-Carlo method. We select random column densities, with replacement, from the sample of measured column densities for all of our Mg II absorbers until we reach the sample size. We then recalculate the column density distribution, find the best parameterized Schechter fit, and then integrate and compute Equation 6.2. We perfom this task 1499 times to develop a statistical ensemble of values for Ω, with this number of samples representing the underlying scatter in the $\Omega_{\mathrm{Mg\,II}}$ distribution at the 99% confidence level according to **?**. We take the standard deviation about the mean of this ensemble of simulated measurements as the 1σ uncertainty in Ω_{MgII}. We find that the cosmic mass density of Mg II increases from $\Omega_{\mathrm{Mg\,II}} \simeq 0.8 \times 10^{-8}$ at $z \sim 0.5$ to $\Omega_{\mathrm{Mg\,II}} \simeq 1.3 \times 10^{-8}$ at $z \sim 2$.
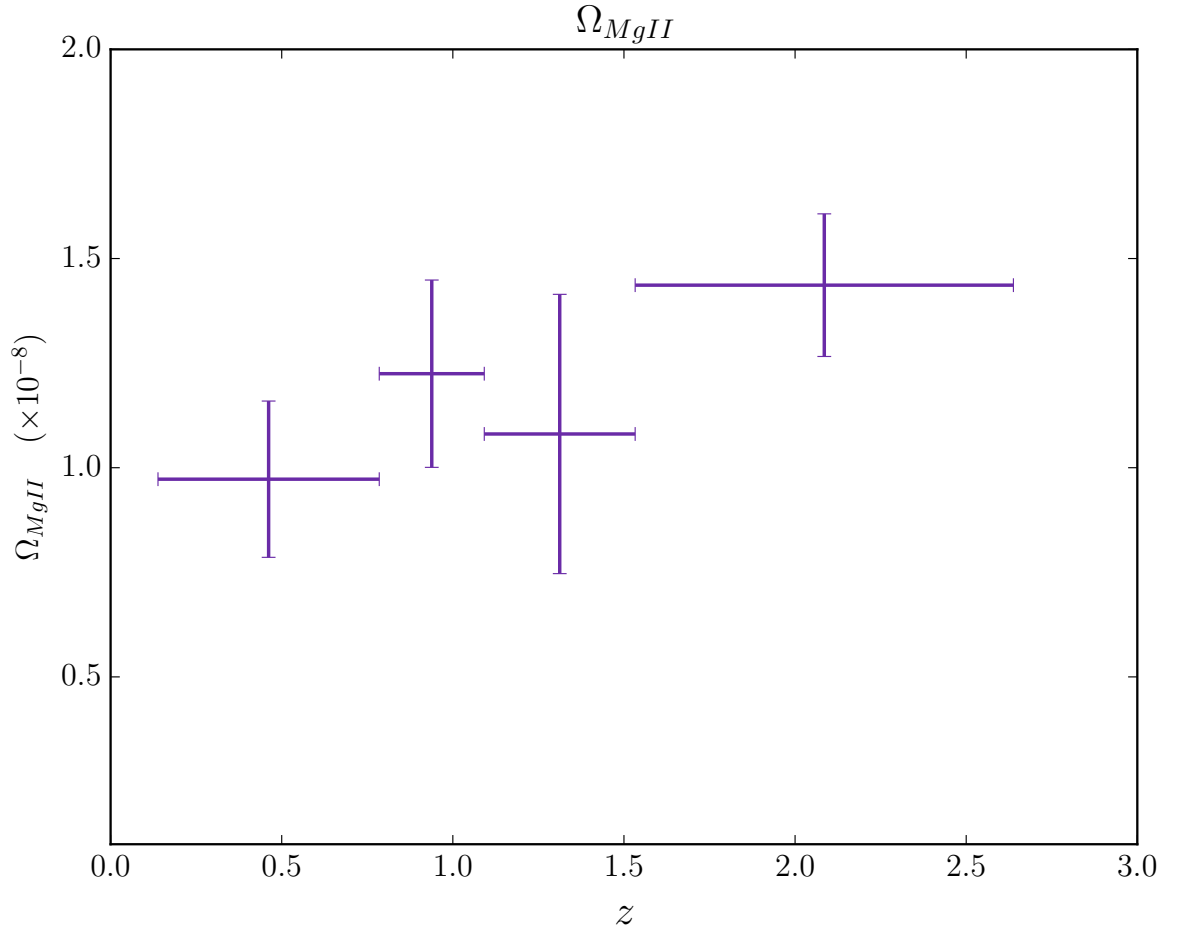
Fig. 5.5.— Ω_{MgII} as a function of redshift. The cosmic mass density of Mg II stays roughly flat near a value of 1×10^{-8}, with a 0.5 dex increase from $z \sim 0.5$ to $z \sim 2$.

5.5. Assessing Possible Sightline Bias in the Mg II Sample

The archival quasar spectra used to construct The Vulture Survey were ob-

served for a multitude of reasons. In cases where observations were taken to target

a previously known absorption line system, these detections could bias our sam-

ple when calculating $d\mathcal{N}/dz$ and $d\mathcal{N}/dX$. Because early studies which discovered

Mg II absorbers did not have the sensitivity to detect weak, low equivalent width
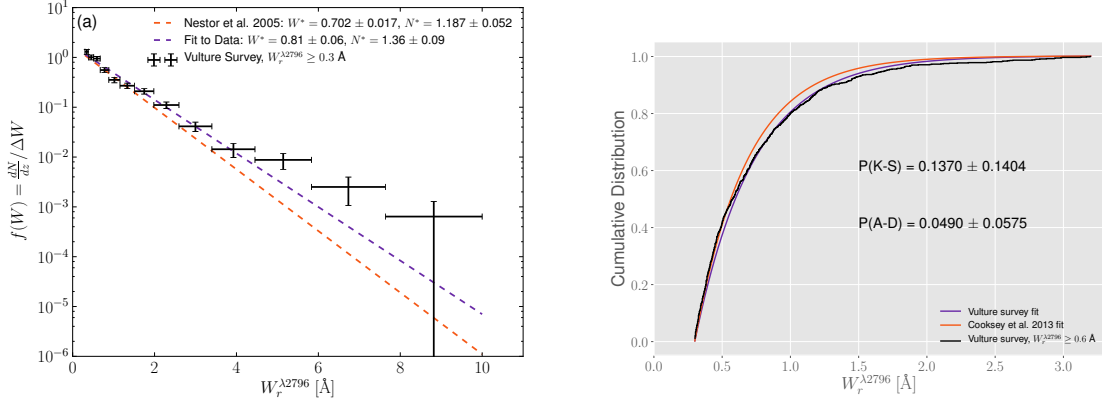
Fig. 5.6.— (a) The $W_r^{\lambda 2796} \geq 0.3$ Å equivalent width frequency distribution for The Vulture Survey in black compared to the exponential fit of Nestor et al. (2005), shown as the orange dashed line, and an exponential fit to The Vulture Survey data in purple. The exponential fits are of the form shown in Equation 5.11. (b) The cumulative distribution of The Vulture Survey data and two comparative exponential fits. The P(K-S) value shown compares our survey's data to the fit from Nestor et al. (2005).

systems, quasar spectra were never selected based upon the presence of weak absorption. However, some spectra were selected based on the presence of strong, $W_r^{\lambda 2796} > 0.3$ Å systems. In order to properly quantify any bias, we compare our work to the large, unbiased sample of the Sloan Digital Sky Survey (SDSS). Specifically, we turn to the work of Nestor et al. (2005) who inventoried strong Mg II absorbers in SDSS quasar spectra. This study employed analysis most similar to our own, identifying absorbers down to $W_r^{\lambda 2796} = 0.3$ Å, and produced parametric fits to the equivalent width frequency distribution, allowing for robust comparisons. These authors analyzed the SDSS Early Data Release; however, modern studies have since used larger samples from subsequent SDSS data releases (**?**Lundgren et al. 2009; **?**; **?**; **?**; **?**). **?** specificallty noted that the Nestor et al. (2005) sample is entirely consistent with their DR7 study.

In Nestor et al. (2005), the authors constructed the equivalent width fre-

quency distribution for absorbers with $W_r^{\lambda2796} > 0.3$ Å and found the best fit to this distribution was an exponential function of the form,

$$f(W_r^{\lambda2796}) = \frac{N^*}{W^*}e^{-\left(W_r^{\lambda2796}/W^*\right)} \tag{5.11}$$

where N^* and W^* are constants. In order to compare to the SDSS data, we limit our sample to absorbers with equivalent widths $W_r^{\lambda2796} > 0.3$ Å and calculate the equivalent width frequency distribution. In Figure 5.6(a), we show $f(W_r^{\lambda2796})$ for The Vulture Survey and an exponential fit to our data, along with the exponential fit of Nestor et al. (2005). Nestor et al. (2005) found the best-fit parameters and corresponding 1σ uncertainties to be $N^* = 1.187 \pm 0.052$ and $W^* = 0.702 \pm 0.017$. When we perform the same analysis, fitting Equation 5.11 to The Vulture Survey data, we derive $N^* = 1.39 \pm 0.10$ and $W^* = 0.74 \pm 0.05$. By eye, there appears a slight excess in the number of Mg II absorbers above $W_r^{\lambda2796} > 3$ Å, with the frequency of these absorbers roughly 2σ higher than the Nestor et al. (2005) exponential fit.

In order to statistically determine the bias in our sample, we perform a Kolmogorov–Smirnov (KS) test to quantitatively measure the similarity between our sample of absorbers with $W_r^{\lambda2796} > 0.3$ Å and the SDSS sample of Nestor et al. (2005). We first sample a population of 1331 measured absorber equivalent widths, matching the SDSS sample size, from the exponential fit to the equivalent width ditribution of Nestor et al. (2005), incorporating the reported 1σ scatter in the fit parameters. This allows us to directly compare to the sample of measured Mg II equivalent widths from The Vulture Survey.

In Figure 5.6(b), we show the cumulative distribution of the strong absorbers

in The Vulture Survey in black, along with the exponential fit to our data and the fit of Nestor et al. (2005). We then perform a two-sample KS test, calculating the P-value, which is the probability that the two samples are drawn from different underlying distributions, defined as P(K-S). To avoid issues due to the random resampling of the Nestor et al. (2005) distribution, we repeat this exercise one million times as a Monte-Carlo method, generating an ensemble of P(K-S) values. We take the mean P(K-S) value as the true probability that the samples are inconsistent, and the standard deviation about this mean as the 1σ uncertainty. Our criterion to assert that our sample is consistent with an unbiased sample requires P(K-S) > 0.0027, which means that it could not be ruled out at the 3σ level that the two populations are consistent with one another. With P(K-S) = 0.112 ± 0.049, and only one instance out of the million Monte-Carlo runs exhibiting a P(K-S) value below 0.0027, we conclude that our sample is consistent with an unbiased sample, even at the 2σ level, and that the strong absorbers in The Vulture Survey could very well have originated from the same underlying population as the unbiased SDSS quasar spectra sample.

5.6. Strong vs. Weak Absorbers

We have shown a cosmic inventory of Mg II absorbing gas from $0.1 < z < 2.6$, measuring $d\mathcal{N}/dz$, $d\mathcal{N}/dX$, the equivalent width distribution, and the column density distribution down to detection limits as low as $W_r^{\lambda 2796} = 0.01$ Å. We aim now to relate the properties of Mg II absorbers and their evolution across cosmic time to other known evolutionary processes with the hope of gaining insight into the mechanisms which give rise to Mg II absorbing gas.

Narayanan et al. (2007) measured the evolution of weak Mg II absorbers from $0.4 < z < 2.4$ in VLT/UVES spectra. They compared to Churchill et al. (1999), who fitted the equivalent width frequency distribution with a power-law, and to Nestor et al. (2005), who fitted an exponential to $f(W_r)$. In the case of weak absorbers at $z < 1.4$, Narayanan et al. (2007) found that a power-law with a slope of $\alpha = -1.04$ is a satisfactory fit, confirming the results of Churchill et al. (1999). When they split their sample into low redshift, with detections between $0.4 < z < 1.4$, and high redshift, with detections between $1.4 < z < 2.4$, they found that the low redshfit sample remained consistent with a power-law but the high redshift sample was best fit by an exponential function. Our data show that a faint end power-law slope of $\alpha = -0.81$ is appropriate for the higher redshift subsample, and we note that this is also consistent with the data of Narayanan et al. (2007).

Narayanan et al. (2007) also analyzed the evolution of $d\mathcal{N}/dz$ with redshift for weak Mg II absorbers. They found that the distribution follows the "no evolution" expectation; that is, the expected number density for a nonevolving population of absorbers in a ΛCDM universe, at redshifts less than $z = 1.5$. At higher redshift, they found that $d\mathcal{N}/dz$ for weak absorbers decreases below the no evolution expectation. In Figure 5.7(a) we make a direct comparison with Narayanan et al. (2007), showing $d\mathcal{N}/dz$ for $0.02 \leq W_r^{\lambda 2796} < 0.3$ Å binned in the same manner as their Figure 4. Here, we observe that the apparent peak in $d\mathcal{N}/dz$ for weak absorbers occurs near $z = 0.75$, as opposed to $z = 1.2$ in Narayanan et al. (2007). However, the overall shape of $d\mathcal{N}/dz$ for this low equivalent width population remains in good agreement, with the number of weak absorbers per redshift path length rising from $z = 0.4$ to $z \sim 1.0$, following the no evolution expectation, and

then falling well below that expectation from $z \sim 1.0$ to $z \sim 2.4$.

In Figure 5.7(b), we show $d\mathcal{N}/dX$ for weak Mg II absorbers. Here, we clearly see evolution in the distribution of low equivalent width absorbers, showing that the comoving line density of weak Mg II absorbers steadily decreases as a function of redshift from $z = 0.4$ to $z = 2.4$. The "no evolution" assumption would be a perfectly flat distribution, as shown by the solid red line. We also fit a linear approximation to the binned data of Figure 5.7(b) of the form $d\mathcal{N}/dX = -0.28\,(\pm 0.04)z + 0.92\,(\pm 0.04)$, including the lowest redshift data point taken from **?**. This function shows $d\mathcal{N}/dX$ going to zero at $z = 3.3$, implying that no Mg II absorbers with equivalent widths between $0.02 < W_r^{\lambda 2796} \leq 0.3$ Å should be detected above this redshift. In other words, weak Mg II absorbers are predicted not to exist at redshifts above $z = 3.3$ by this trend. This evolution follows similar trends to the evolution in cosmic metallicity and ionizing background intensity, such that we detect more weak Mg II absorbers at low redshift, where the metallicity of the CGM is higher and the ionizing background is less likely to destroy Mg II, as opposed to higher redshifts, where the opposite applies.

Steidel & Sargent (1992), and later Nestor et al. (2005), examined the redshift evolution of $d\mathcal{N}/dz$ for strong Mg II absorbers with $W_r^{\lambda 2796} > 0.3$ Å. They found that the number of strong Mg II absorbers per redshift path length increases as a function of redshift from $z = 0$ to $z = 2.2$; however, they could not derive the slope of this trend to sufficient accuracy to distinguish between an evolving population or a non-evolving population. We perform a similar analysis on our sample, calculating instead $d\mathcal{N}/dX$, where a flat distribution implies no evolution. When we take absorbers with $W_r^{\lambda 2796} > 0.3$ Å, we find that a fit to the function $d\mathcal{N}/dX = \frac{c}{H_o} n_0\,\sigma_0(1+z)^\epsilon$ with a slope of $\epsilon = -0.20 \pm 0.22$ is appropriate, implying

that the comoving number density and/or cross-section of strong Mg II absorbers does not significantly evolve. However, when considering even stronger absorbers with $W_r^{\lambda 2796} > 1$ Å, we do observe evolution in $d\mathcal{N}/dX$, with the evolution parameter, ϵ, becomming positive and increasing, as shown in Figure 5.2.

This evolution does not seem to be influenced by either an increase in the cosmic metallicity at low redshifts, or a decrease in the intensity of the cosmic ionizing background near the present epoch, which should produce more favorable conditions for Mg II absorbing gas. In fact, in order to seemingly oppose these factors, we must infer an increase in the total quantity of Mg II absorbing gas, observed as high equivalent width Mg II systems, outside galaxies near $z = 2$. In Section 5.6.2, we will explore the physical processes responsible for evolution in the universal distribution of Mg II absorbing gas.

5.6.1. Total Equivalent Width Distribution

? combined multiple previous studies to characterize the equivalent width distribution function, $f(W_r)$. It is important to note, for comparison, that their sample with $W_r < 0.3$ Å spans redshifts from $0.4 \le z \le 1.4$, while their sample with $W_r \ge 0.3$ Å spans $0.4 \le z \le 2.3$. They found a Schechter function with a low equivalent width slope of $\alpha = -0.642 \pm 0.062$ and a characteristic equivalent width for the exponential cutoff of $W^* = 0.97 \pm 0.06$ Å best fit the data, within the reported 1σ uncertainties. In Figure 5.8, we perform the same analysis with the total sample of our survey, finding $\alpha = -0.91 \pm 0.04$ and $W^* = 1.69 \pm 0.26$ Å. The point of tension between these studies lies in the value of the low equivalent width slope. ? combine very different surveys in order to sample the full equivalent width

distribution, leading to a non-uniform data set. Specifically at the low equivalent end of the distribution, we note that the error in their determination of α is smaller than the scatter in the data. In private communication with the authors, they speculate that differences in the analysis methods of low equivalent width Mg II absorption line surveys lead to unaccounted systematics and an underestimation of the error in their functional fits.

At redshifts beyond $z \sim 2.5$, the works of Matejek & Simcoe (2012), Matejek et al. (2013), and Chen et al. (2016) described the detection statistics of strong Mg II absorbers up to $z = 7$ using the Magellan/FIRE spectrograph. They found that $d\mathcal{N}/dX$ for all absorbers with $W_r^{\lambda 2796} > 0.3$ Å does not evolve from $z = 0.25$ to $z = 7$. However, restricting their sample to the absorbers with $W_r^{\lambda 2796} > 1.0$ Å, they found approximately a factor of 2 increase in number density at $z = 2 - 3$ compared to $z = 0$. At redshifts above $z = 3$, $d\mathcal{N}/dX$ declines by an order of magnitude by $z \sim 6$. Converting Mg II equivalent widths into an effective contribution to the global star formation rate using the methods of **?** and comparing them to the total galaxy star formation rate density derived from observations of deep fields, they found exceptional agreement in the evolutionary trends of both distributions at all redshifts. The incidence of strong Mg II absorbers at all redshifts is tied to star formation.

5.6.2. Potential Causes for Trends

The most obvious conclusion to be drawn from our analysis of Mg II absorbers in The Vulture Survey is that the physical conditions affecting Mg II absorbers change as a function of redshift. When we compare the sample of Mg II absorbers

at $z \sim 0.5$ to the sample of absorbers at $z \sim 2$, we find the following statements are true of the higher redshift sample:

1. There are more strong Mg II absorbers per redshift path length and per absorption path.

2. The faint end slope of the equivalent width and column density distributions is flatter.

3. The "knee" of the Shechter fit to the equivalent width and column density distributions lies at higher values of $W_r^{\lambda 2796}$ and $N(\text{Mg II})$.

4. The cosmic mass density of Mg II is larger.

We can now state that the physical properties driving the global distribution of Mg II absorbers at $z \sim 0.5$ are different than at $z \sim 2$. In addition, these physical properties do not affect all Mg II systems equally. If we examine weak systems alone, we find that these low equivalent width absorbers follow a no-evolution expectation from present day up to $z \sim 1$, at which point they decrease in number per absorption path length rapidly until $z \sim 2.5$. If we examine the strongest systems, those with $W_r^{\lambda 2796} > 1.0$ Å, we find the opposite behavior, where these absorbers are more numerous at $z \sim 2.5$ than at $z \sim 0.5$. The properties of a given Mg II absorbing cloud are governed by the nature of the radiation incident on the cloud, the gas phase metallicity, and the total amount of gas present. Therefore, possible explanations relate to the ionization conditions in the halos of galaxies at this time, the metallicity of gas located in the circumgalactic medium, and/or the quantity of metals around galaxies, which we will now explore.

5.6.3. Ionization Conditions

Haardt & Madau (2012) represents the most recent estimate of the cosmic ionizing background as a function of redshift, which is the primary ionizing component responsible for the universal ionization state of gas in galactic halos. Mg II absorbers are subject primarily to this UV background, with very little contribution from stellar radiation from a nearby galaxy (Churchill et al. 1999; **?**; **?**). The ionization state of magnesium is governed predominantly by the ionization balance of photons of energies near 7.6 eV (0.56 Ryd), which ionizes Mg I, and near 15.035 eV (1.1 Ryd), which ionizes Mg II. The authors found that the comoving emissivity near 7.6 eV is roughly three times higher at $z = 3.1$ than at $z = 1.0$, implying that Mg II is created more readily near $z = 3.1$. However, the comoving emissivity at 15 eV is two orders of magnitude higher at $z = 3.1$ than at $z = 1.0$, which leads to the preferential ionization of Mg II near $z = 3.1$. The number of these ionizing 15.035 eV photons drives the ionization state of Mg II as a function of redshift.

As the number of ionizing photons in the IGM increases with increasing redshift, holding constant the density and quantity of metals in galactic halos, we would nominally expect for the ionization parameter of Mg II absorbers in the halos of galaxies to increase with redshift. Increasing the ionization parameter alone should decrease the observed quantity of Mg II, as it favors lower ionization parameter conditions. The comoving line density ($d\mathcal{N}/dX$) of Mg II absorbers with equivalent widths below $W_r^{\lambda 2796} < 0.3$ Å declines linearly with increasing redshift, following the expectation that a more intense ionizing background at higher redshift disfavors Mg II absorption. However, when examining absorbers

with $W_r^{\lambda 2796} > 0.3$ Å, we observe the opposite trend. These strong systems are not less numerous at higher redshift as a result of harsh ionizing conditions in the halos of galaxies. We therefore disfavor the hypothesis that changes in ionzation conditions in the halos of galaxies predominantly drive the observed enhancement in the number of strong MgII absorbers at redshift $z \sim 2$ compared to $z \sim 0.5$.

5.6.4. Metallicity

The metallicity of the CGM has been best characterized by studies of damped Lyα absorbers (DLAs; neutral hydrogen absorbers with $\log(N(\mathrm{HI})) > 20.3$) and sub-DLAs ($19.0$ cm$^{-2} < \log(N(\mathrm{HI})) < 20.3$ cm^{-2}) located in the halos of galaxies, where many metal line transitions are observable, such as **?**, **?**, and **?**. They found a rough trend of decreasing metallicity with increasing redshift dominated by scatter. These high column density systems certainly do not trace all ionized gas in the halos of galaxies as DLAs are predominantly neutral. Using a sample of gravitationally lensed galaxies, it has also been shown that the overall gas phase metallicity of star forming galaxies is 0.35 dex lower at $z \sim 2$ than at $z \sim 0$ (**?**). In addition, **?** and **?** examined Lyman Limit Systems (LLS) and found that at $0.1 \leq z \leq 1.1$, the metallicity distribution is bimodal with peaks at $[X/H] \simeq -1.8$ and -0.3. At $z \geq 2$, they found a unimodal distribution with a peak at $[X/H] \simeq -2$.

Many links exist between neutral hydrogen absorption and MgII absorbers. Specifically, **?** show that a correlation exists between the neutral hydrogen column density of an absorber and the rest frame MgII equivalent width, with stronger MgII absorbing systems having large HI column densities. As MgII absorbers are

often found associated with nearby galaxies, one can expect that the metallicity evolution of DLAs and sub-DLAs should be reflected in the evolution of Mg$\textsc{ii}$ absorbing systems (**????**).

Assuming, then, that over time the overall metallicity of the circumgalactic medium increases, it would not be expected to observe larger quantities of Mg$\textsc{ii}$ at $z \sim 2$ compared to $z \sim 0$. In fact, metals should build up over time in the halos of galaxies, producing more Mg$\textsc{ii}$ absorption at lower redshift. We can better understand the role of metallicity by again comparing the sample of weak Mg$\textsc{ii}$ absorbers to strong Mg$\textsc{ii}$ absorbers. The weak systems follow the trend of rising CGM metallicity with time, by having a higher $d\mathcal{N}/dX$ at $z \sim 0$ as compared to $z \sim 2$. However, the strongest Mg$\textsc{ii}$ systems evolve in an opposite manner to trends in cosmic metallicity, implying that other physical properties drive their evolution. Furthermore, these very high equivalent width systems have the highest column densities, and with these strong systems being more numerous at higher redshifts, they drive the cosmic matter density of Mg$\textsc{ii}$ absorbing gas to its highest value at $z \sim 2$. Cosmic metallicity evolution alone, then, cannot explain the slightly enhanced cosmic mass density of Mg$\textsc{ii}$ absorbing gas at $z \sim 2$ as compared to $z \sim 0$.

5.6.5. *Quantity of Magnesium*

This leaves us, then, with the most likely conclusion being that galaxies eject more gas into their halos at $z \sim 2$ than at any other time in the form of strong, high equivalent width absorbers. **?** combined galaxy star formation rate measurements from 19 independent studies from $2006 - 2012$, spanning redshifts

from $0 < z < 8$, to examine evolution in the cosmic star formation rate. They found that galaxies at $z \sim 2$ were forming stars at rates ten times greater than at $z = 0$. In conjunction with the fact that galactic-scale winds can be driven by star formation (**?**), it follows that galaxies were ejecting more metal-enriched gas at $z \sim 2$ than at present through supernovae-driven outflows (**?**Kacprzak et al. 2012; Nestor et al. 2011). Under the assumption that these outflows are observable as Mg II absorption systems, they should manifenst themselves in the form of high equivalent width, high column density Mg II absorbers, dense enough to be shielded from the more intense ionizing background at $z \sim 2$, enhanced in metallicity due to their supernovae origins. Therefore, despite competing factors such as a more intense ionizing background and lower overall cosmic metallicity at higher redshifts, we should measure a larger value of $\Omega_{\mathrm{Mg II}}$ at $z \sim 2$ than at present as a result of galaxy feedback processes ejecting large quantities of Mg II absorbing gas into their halos.

Strong Mg II absorbers still exist at low redshift—their comoving line density does not go to zero at any point in time. However, at low redshifts near the present epoch, the majority of Mg II absorbers are weak, low equivalent width, low column density systems whose properties are likely governed more by metallicity and incident radiation, due to their lower densities disfavoring any self-shielding. These weak absorbers may represent a population of either fragmented outflows, strong systems weathered away in hot halos (**?**), or newly condensed gas in the halos of galaxies (**?**).

Their eventual fate may be to accrete onto their host galaxy, but this rate of accretion must be small compared to the rate at which the cosmic ionizing background weakens and the cosmic metallicity of the halo increases towards lower

redshifts. In other words, the rate of creation of weak Mg II absorbers over time from $z \sim 2$ to the present epoch is greater than the rate of destruction, and this rate of creation may not be tied to an increased quantity of Mg II absorbing gas in the halos of galaxies, but instead an evolution in cosmic properties governing the ionization state of all gas in galactic halos. We must now ask why the weakest systems build up slowly from $z > 2$ to the present epoch, directly opposing the trends observed for the strongest systems. To answer this question, we must understand the innate physical similarities and differences between high equivalent, high column density absorbers and low equivalent width, low column density absorbers.

Studies associated with COS-Halos (Tumlinson et al. 2011) seeking to understand the distribution of metals around galaxies have found the majority of cool, metal absorbing gas lies within the virial radius of galaxies (**?**). **?** also found that the mean cool gas density profile around galaxies scales as R^{-1}, with most strong, low ionization metal absorbers existing near the galaxy itself. Further refining these assertions specifically for Mg II, Churchill et al. (2013a) found that the covering fraction of Mg II absorbers falls to 0 at projected distances beyond the virial radius. This means that the Mg II absorbers observed in The Vulture Survey likely lie within the virial radius of a galaxy. The Mg II absorbing gas observed near $z \sim 2$ should eventually fall onto its host galaxy, or stall at large radii and remain a permanent part of the host galaxy halo (Oppenheimer et al. 2010; **?**). What we observe in the form of low redshift Mg II absorbers therefore may not only be the result of outflows near the present epoch, but also the remnants of the most energetic star-forming period in cosmic history.

Perhaps the most clear-cut evidence that many very strong ($W_r^{\lambda 2796} > 1.0$ Å)

absorbers have their origins in star formation driven winds comes from the works of Matejek & Simcoe (2012) and Chen et al. (2016). The authors examined their sample of high equivalent width Mg II absorbers spanning redshifts $2 < z < 7$, combined with samples from Nestor et al. (2005) and **?** with data below $z < 2$, to relate the Mg II population distribution with the cosmic star formation rate density. Following the methods of **?**, they convert the Mg II rest frame equivalent widths to a comoving [O II] luminosity density, and from there derive a star formation rate density. When these Mg II-derived star formation rate densities were compared with the mean galaxy specific star formation rates from $0 < z < 7$, they found remarkable agreement. We therefore corroborate their results, finding good agreement between the evolutionary behavior of $d\mathcal{N}/dX$ for strong Mg II absorbers and the cosmic star formation rate density. These high equivalent width Mg II systems are preferentially produced by feedback processes associated with star formation.

Referring back to Figure 5.2(a), we can examine how $\frac{c}{H_o} n_0 \sigma_0$ changes for absorbers of different equivalent widths. Here, we can infer that the physical parameter causing $d\mathcal{N}/dX$ to fall between $z \sim 0$ to $z \sim 2$ is the number density of weak Mg II absorbers in galaxy halos (n_0), instead of the absorbing cross-section (σ_0). In **?**, the authors use Cloudy (**?**) to estimate the size and number densities of clouds giving rise to Mg II absorption. According to these simulations, absorber sizes are roughly an order of magnitude smaller at $z \sim 0$ than they were at $z \sim 2$ for clouds of the same hydrogen density across a wide range of densities. This implies the absorbing cross-section is lower at present than at $z \sim 2$, and, therefore, the number density of weak Mg II absorbers should be the driving factor leading to the enhancement of $d\mathcal{N}/dX$ for low equivalent width systems at the

present epoch.

Furthermore, Churchill et al. (2013b) discussed how the theoretical cooling radius, the radial distance from the center of a halo at which the initial gas density equals the characteristic density at which gas can cool, may serve as an important factor in determining the observational properties of Mg II absorbers. They found that within the cooling radius, the covering fraction of Mg II absorption increases, and does so most dramatically for absorbers with equivalent widths below $W_r^{\lambda 2796} = 0.3$ Å. At equivalent widths above this level, covering fractions inside and outside the cooling radius are statistically similar. This points toward a possible physical origin for a substantial portion of weak, low equivalent width Mg II absorbers—these clouds cool and condense from collapsing gas clouds within the cooling radius. This gas could have originated from fragmented outflows or infalling material which, over time, met the conditions required to cool enough to be observed as Mg II, instead of a higher, more ionized species.

Given the above considerations, we favor a picture where galaxies, during the most active epoch of star formation in cosmic history, expell large quantities of metal enriched gas into their halos through star formation driven outflows at $z \sim 2$. These outflows manifest themselves in observations as strong Mg II absorbers. Their destiny will be to eventually either fall back onto the galaxy and enrich the ISM or remain in the halo, subject to the cosmic ionizing background and possible fragmentation. Those absorbers which remain intact and accrete onto the galaxy are lost from observations at lower redshifts, while those which remain at larger radii will likely reach equilibrium with the ionization conditions in the halo. As the intensity of the cosmic ionizing background decreases with time, and more metals are ejected into the halo over time, more of this gas appears as

47

weak Mg II absorption near $z \sim 0$. Many of these weak Mg II absorbers are likely more passive in nature, participating less in the overall baryon cycle in and out of galaxies, subject primarily to the environmental conditions of the CGM.
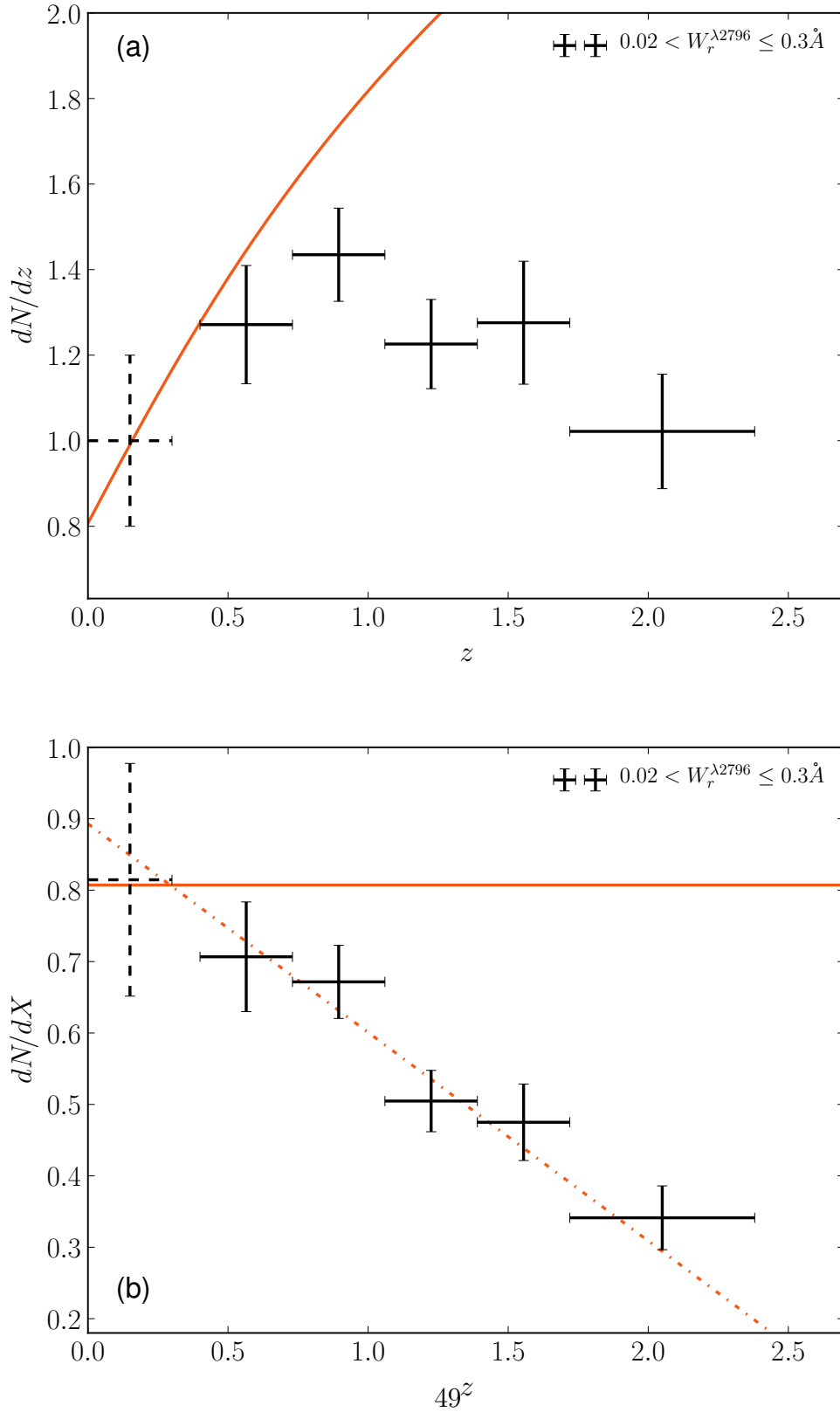
Fig. 5.7.— (a) $d\mathcal{N}/dz$ as a function of redshift for equivalent widths in the range $0.02 < W_r^{\lambda 2796} \leq 0.3$ Å. We also include the survey data point from $0 < z < 0.3$ of ? as shown by the dashed histogram. (b) $d\mathcal{N}/dX$ as a function of redshift for the same population. Error bars represent 1σ uncertainties as calculated in Equations 5.1 and 5.3. The red solid lines represent the no-evolution expectation.
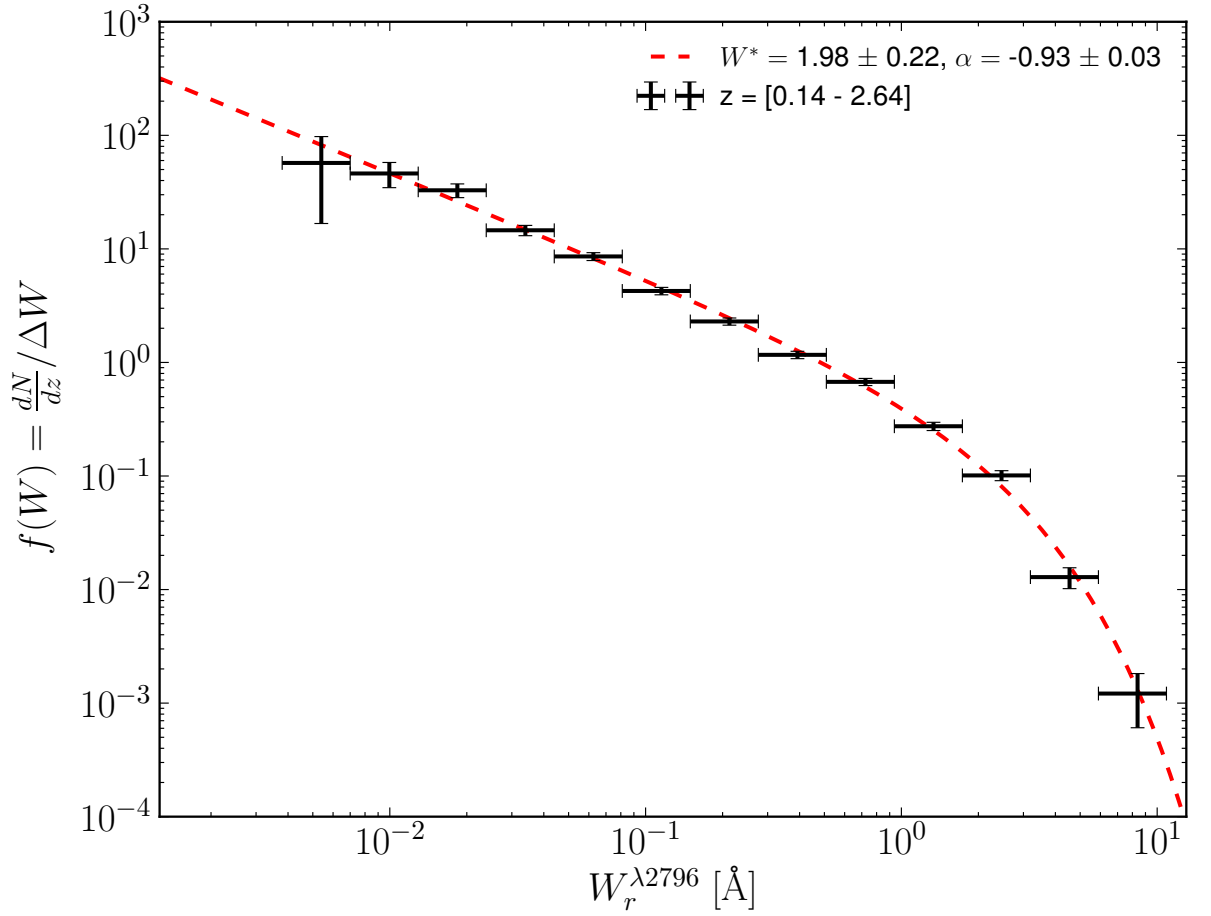
Fig. 5.8.— The equivalent width distribution of all detected Mg II absorbers, defined as the redshift path density $(d\mathcal{N}/dz)$ in each equivalent width bin divided by the bin width. The cosmic distribution of absorbing Mg II is well fit by a Schechter function, with the parameters detailed in Equation 5.9.

6.   PROPERTIES AND EVOLUTION OF CIV ABSORBERS

Now we can finally get down to the science!

6.1.   Number of Absorbers Per Path Length

Previous studies of the statistical properties of CIV absorbers have thoroughly characterized CIV absorbers with equivalent widths above $W_r^{\lambda 1548} = 0.3$ Å. This corresponds to the detection limit of the Sloan Digital Sky Survey (SDSS), which catalogs hundreds of thousands of quasar spectra. Unfortunately, the distribution of the low equivalent width regime of CIV absorbers has not been characterized.

We follow the prescriptions of Paper 1, in which we details the calculations of dN/dz and dN/dX, the redshift path density and absorption path density, respectively. These metrics describe the expected number of detected absorbers through a given redshift or absorption path length.

In Figures 6.1 and 6.2, we plot dN/dz and dN/dX as a function of redshift for varying equivalent width cuts. Dotted lines are fit according to the analytical form which allows for redshift evolution in dN/dX, defined as,

$$\frac{dN}{d(z, X)} = n\sigma(1 + z)^\epsilon,$$ (6.1)

where n is the number density of CIV absorbers, σ is the absorbing cross-section, and ϵ is the power dependence of dN/dX on redshift.

In Figures 6.3 and 6.4, we show the evolution of the Hubble opacity and the evolution parameter as a function of different equivalent width cuts. As we
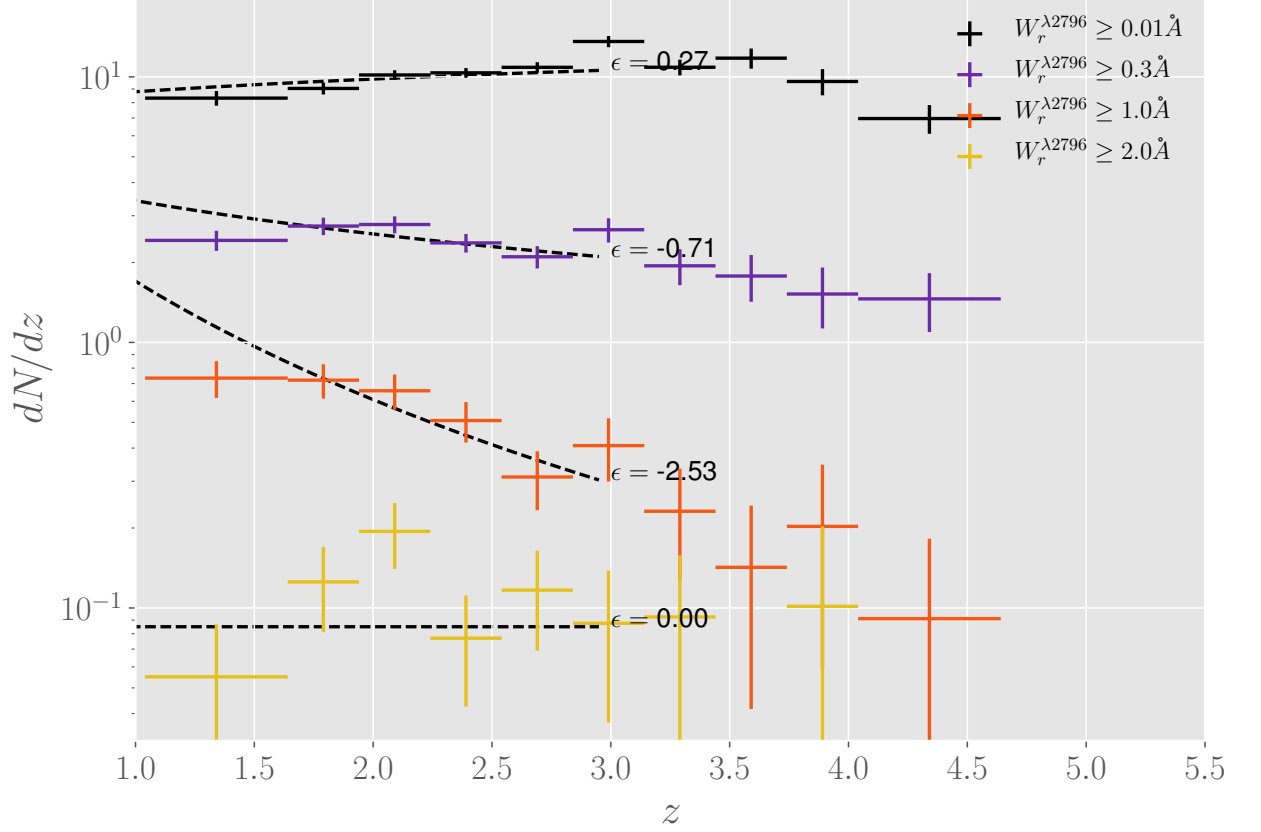
51

Fig. 6.1.— $\frac{dN}{dZ}$ as a function of redshift for varying $W_r^{\lambda 1548}$ cuts. Colors represent different equivalent width cuts. The black dotted lines are fits to the distribution of the functional form $f(z) = n\sigma(1+z)^\epsilon$, with the best fit ϵ value labelled.

apply larger equivalent width cuts, $n\sigma$ stays relatively flat before rising to a peak at $W_r^{\lambda 1548} = 0.7$ Å. This value then drops precipitously, representing a decreasing incidence of very strong CIV absorbers, whether by decreasing number density, absorbing cross-section, or both. In addition, ϵ becomes more negative with increasing equivalent width cuts up until around $W_r^{\lambda 1548} = 0.7$ Å, at which point it rises again for the strongest CIV absorbers. This transition at $W_r^{\lambda 1548} = 0.7$ Å occurs not because the overall slope of the distribution necessarily changes, but

instead because the distribution takes on a different shape not well described by Equation 6.1, where dN/dz and dN/dX peak around $z = 2$, but decrease towards higher and lower redshifts.

6.2. Equivalent Width Distribution

We calculate the equivalent width frequency distribution by first calculating dN/dz and dN/dX for each absorber equivalent width, then summing the distribution in equivalent width bins, and then dividing by the bin width. We examine four redshift bins, requiring that the number of absorbers in each redshift range remains constant.

In Figure 6.6, we plot the equivalent width frequency distribution. We fit this distribution with a Shechter function to parameterize the distribution and to compare the relative differences between varying redshift cuts. We find the low equivalent width slope decreases towards shallower values as redshift increases, implying a decrease in weak C IV absorbers and a relative increase in strong C IV absorbers from low redshift to redshifts near $z = 2$.

6.3. Column Density Distribution

To calculate the column density distribution, we calculate dN/dX for each absorber equivalent width, sum the distribution in column density bins, and then divide by the bin width. The result is a characteristic number density of C IV absorbers per absorption path length as a function of their column densities. It should be noted that at high column densities near $\log(N(CIV)) = 15$, the measured column densities are lower limits as the AOD method to measure column

densities cannot constrain the true column when the line saturates.

In Figure 6.8, we plot the column density frequency distribution. Again, we fit this distribution with a Schechter function. We find again that the low column density end of the distribution becomes shallower as one goes from low redshift to $z = 2$. Due to saturation effects, the final high column density bin is likely best regarded as a lower limit.

6.4. $\Omega_{\mathrm{C\,IV}}$

We now aim to calculate the matter density of C IV absorbers across cosmic time using the following equation,

$$\Omega_{CIV} = \frac{H_0 \, m_{Mg}}{c \, \rho_{c,0}} \int_{N_{min}}^{N_{max}} f(N_{CIV}) \, N_{CIV} \, dN_{CIV}, \tag{6.2}$$

where H_0 is the Hubble constant today, $m_{Mg} = 4.035 \times 10^{-23}$ g, c is the speed of light, $\rho_{c,0}$ is the critical density at present, $f(N_{CIV})$ is the column density distribution of CIV absorbers, and N_{CIV} is the column density. We numerically integrate the Schecter Function fit to $f(N_{CIV})$, multiplied by N_{CIV}. The results are shown below in Figure 6.9.

Errors are derived by bootstrap Monte-Carlo, performing the same sample analysis outlined in Sections **??** and **??** on a random sample, selected with replacement, of C IV absorbers. We take the standard deviation about the mean of this ensemble of random samples as the error in Ω_{CIV}.

54

6.5. Strong vs. Weak Absorbers

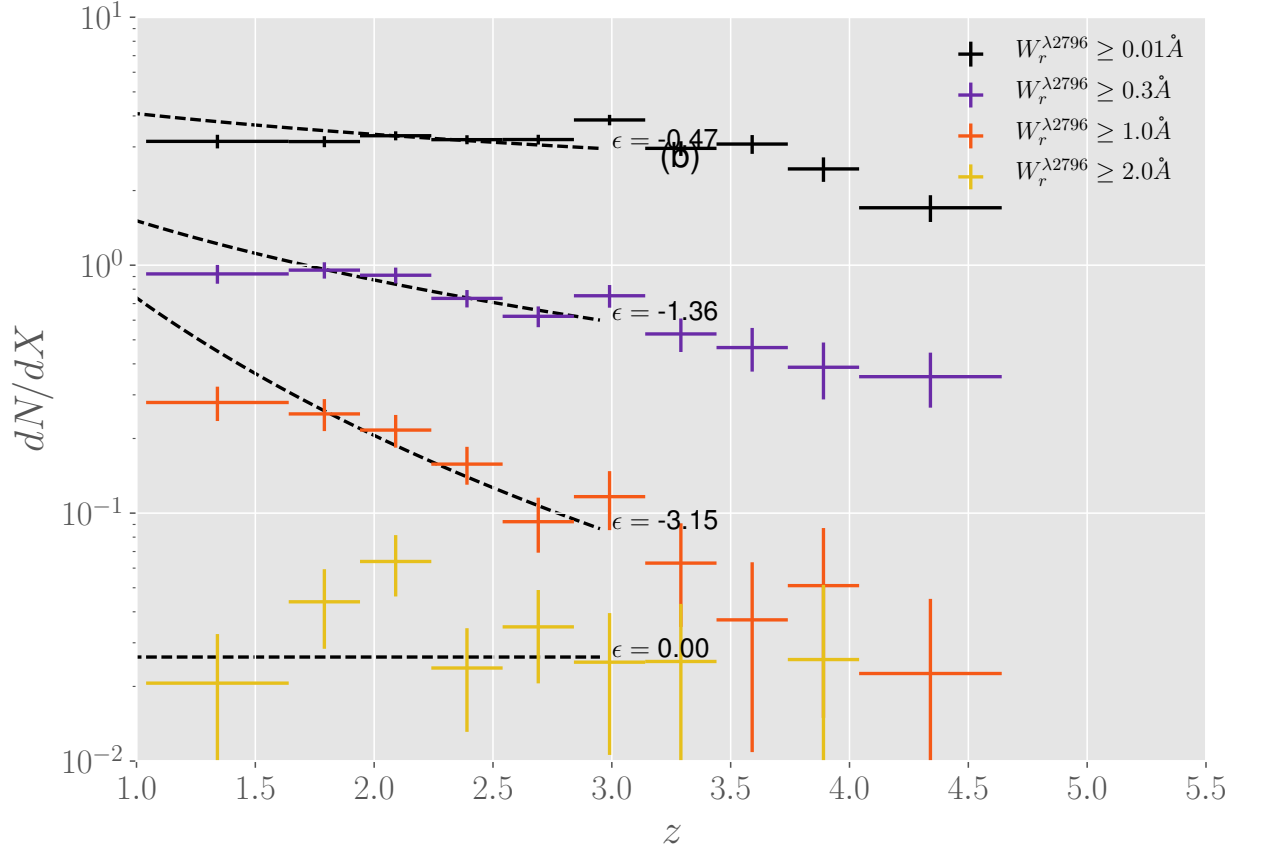Here's where the cool stuff really lies.

Fig. 6.2.— $\frac{dN}{dX}$ as a function of redshift for varying $W_r^{\lambda 1548}$ cuts. Colors represent different equivalent width cuts. The black dotted lines are fits to the distribution of the functional form $f(z) = n\sigma(1+z)^\epsilon$, with the best fit ϵ value labelled. We see increasing values of ϵ with increasing equivalent width, driven by an enhancement of stronger CIV absorbers around redshift 2 compared to lower redshifts.
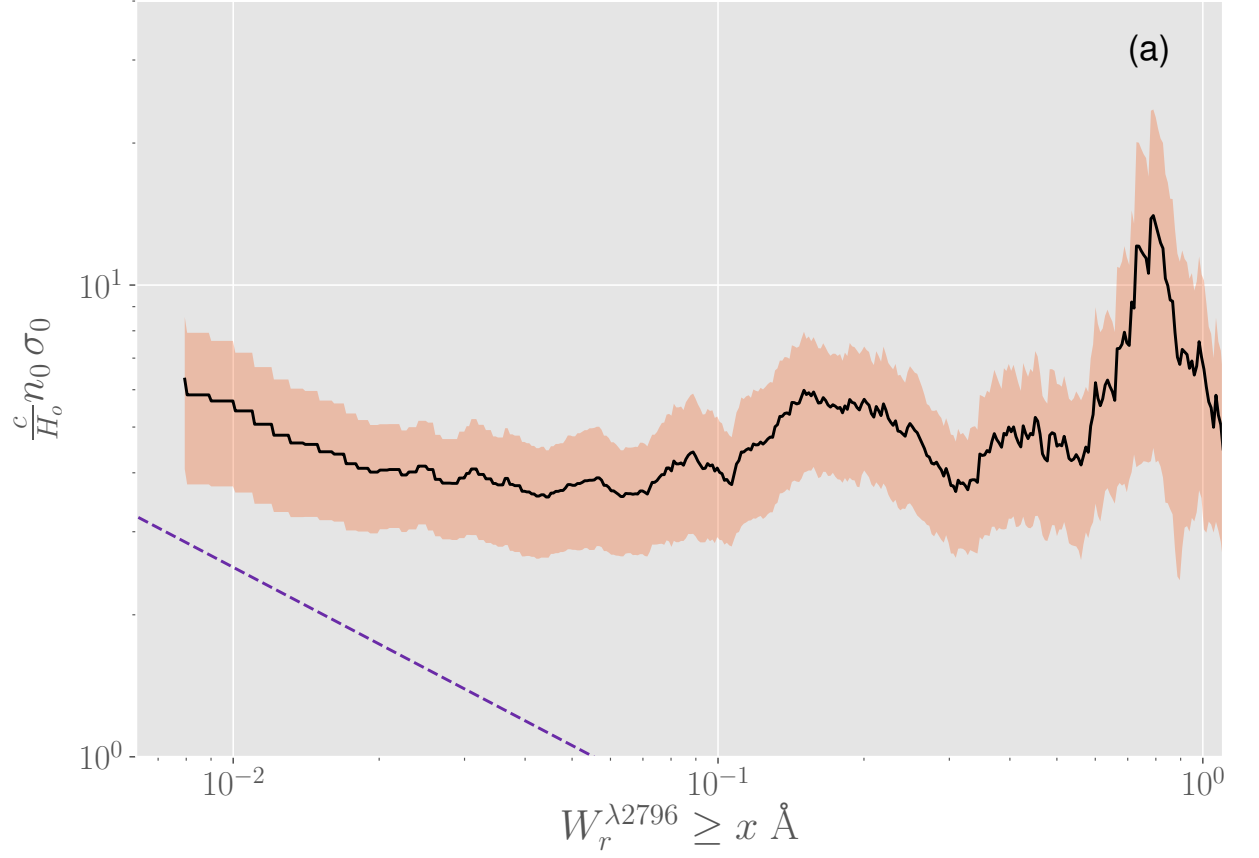
Fig. 6.3.— Absorber space density times cross section, as derived from the funtional fit $dN/dX = n\sigma(1 + z)^\epsilon$ as a function of cumulative equivalent width cut, where $W_r^{\lambda1548} > x$ Å. As C IV equivalent width increases, either the space density of absorbing cloud structures decreses, the absorbing cross-section decreases, or both parameters decrease.
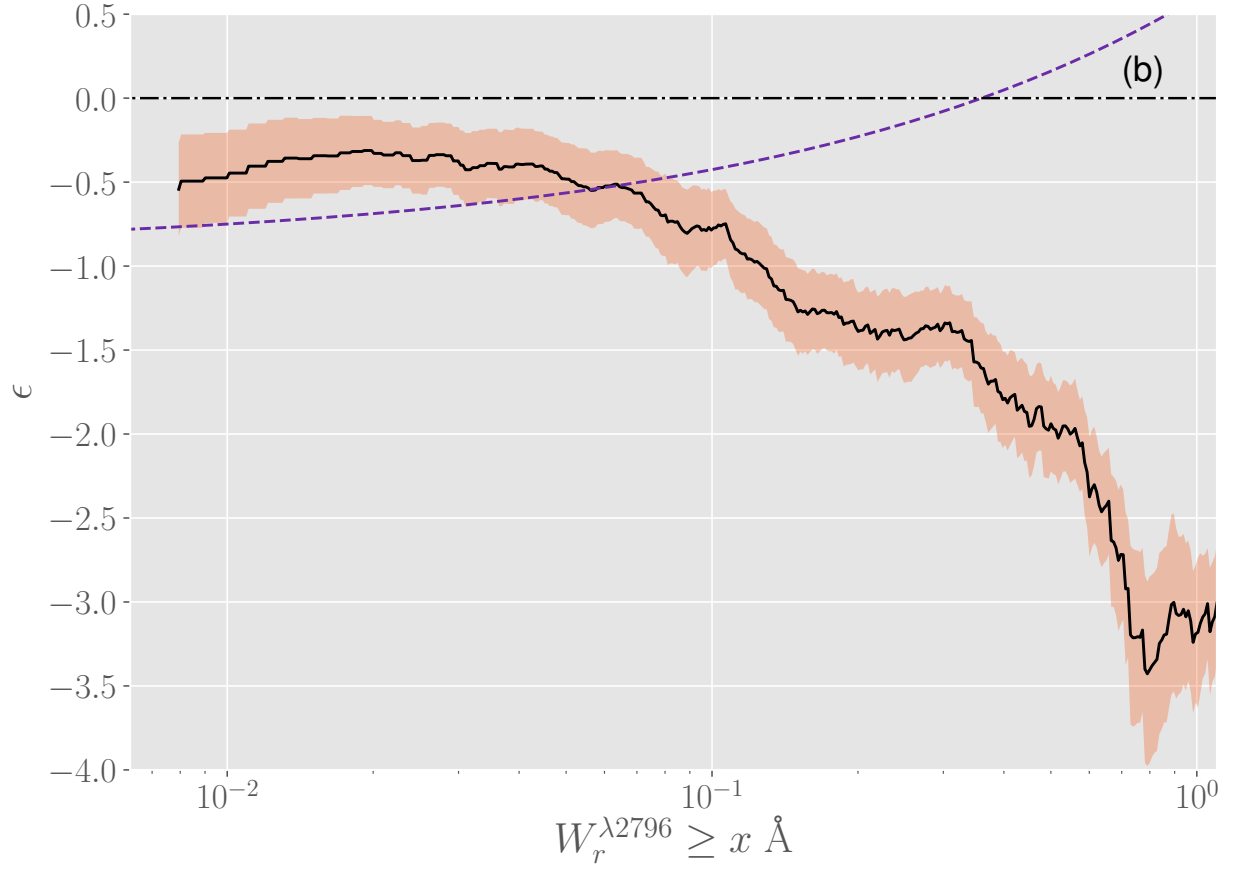
Fig. 6.4.— Redshift power dependence of the functional fit $dN/dX = n\sigma(1+z)^\epsilon$ as a function of cumulative equivalent width cut, where $W_r^{\lambda1548} > x$ Å. Weak CIV absorbers are more abundant at low redshift, leading to a negative coefficient ϵ. Moderate equivalent width CIV absorbers do not evolve, showing $\epsilon \simeq 0$. Strong CIV absorbers evolve away at low redshift, showing a large positive ϵ increasing towards $z = 2$.
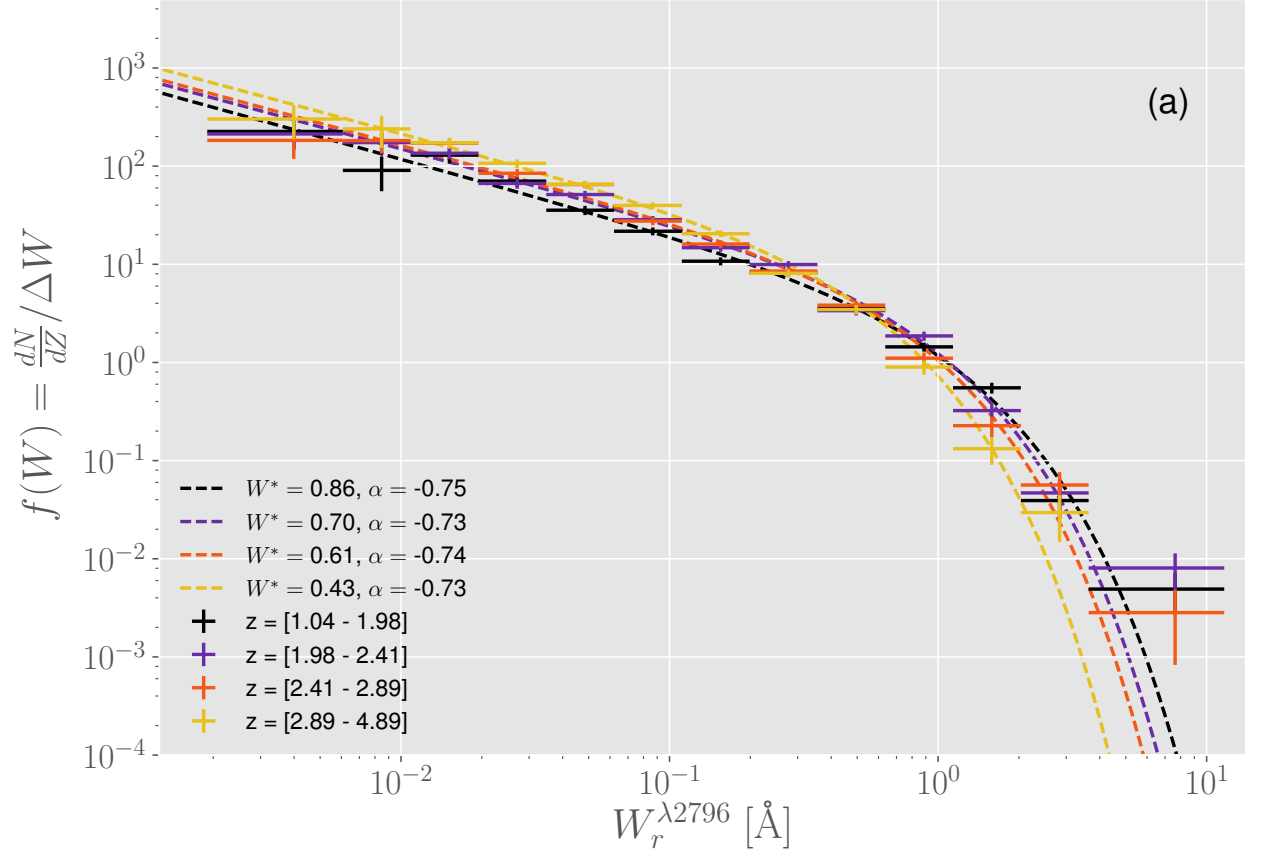
Fig. 6.5.— The equivalent width distribution of C IV absorbers, defined as the comoving line density ($\frac{dN}{dX}$) in each equivalent width bin divided by the bin width. We fit this distribution with a Schechter function, capturing the self-similar power law behavior of the distribution before the exponential cutoff limiting the size of C IV absorbers.
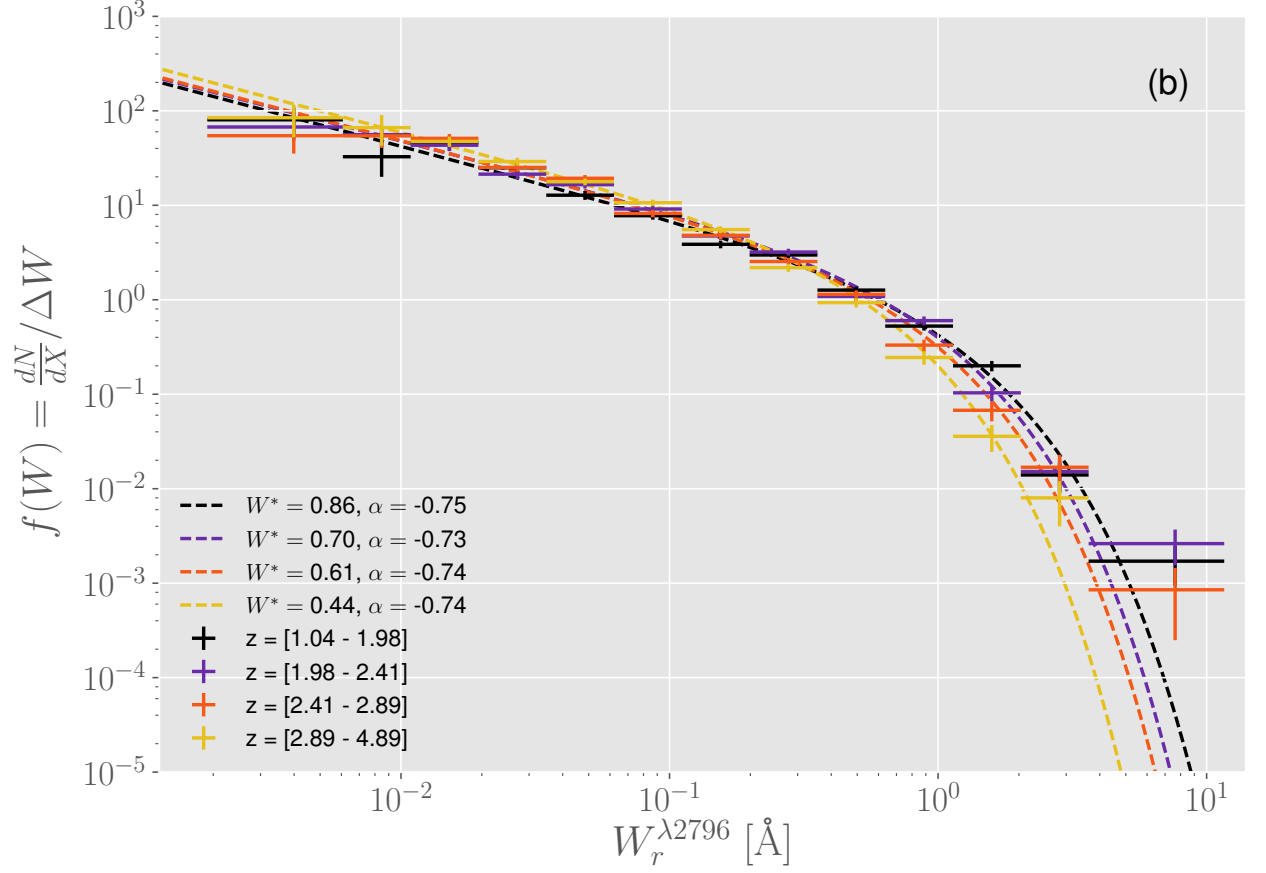
Fig. 6.6.— The equivalent width distribution of C IV absorbers, defined as the comoving line density ($\frac{dN}{dX}$) in each equivalent width bin divided by the bin width. We fit this distribution with a Schechter function, capturing the self-similar power law behavior of the distribution before the exponential cutoff limiting the size of C IV absorbers.
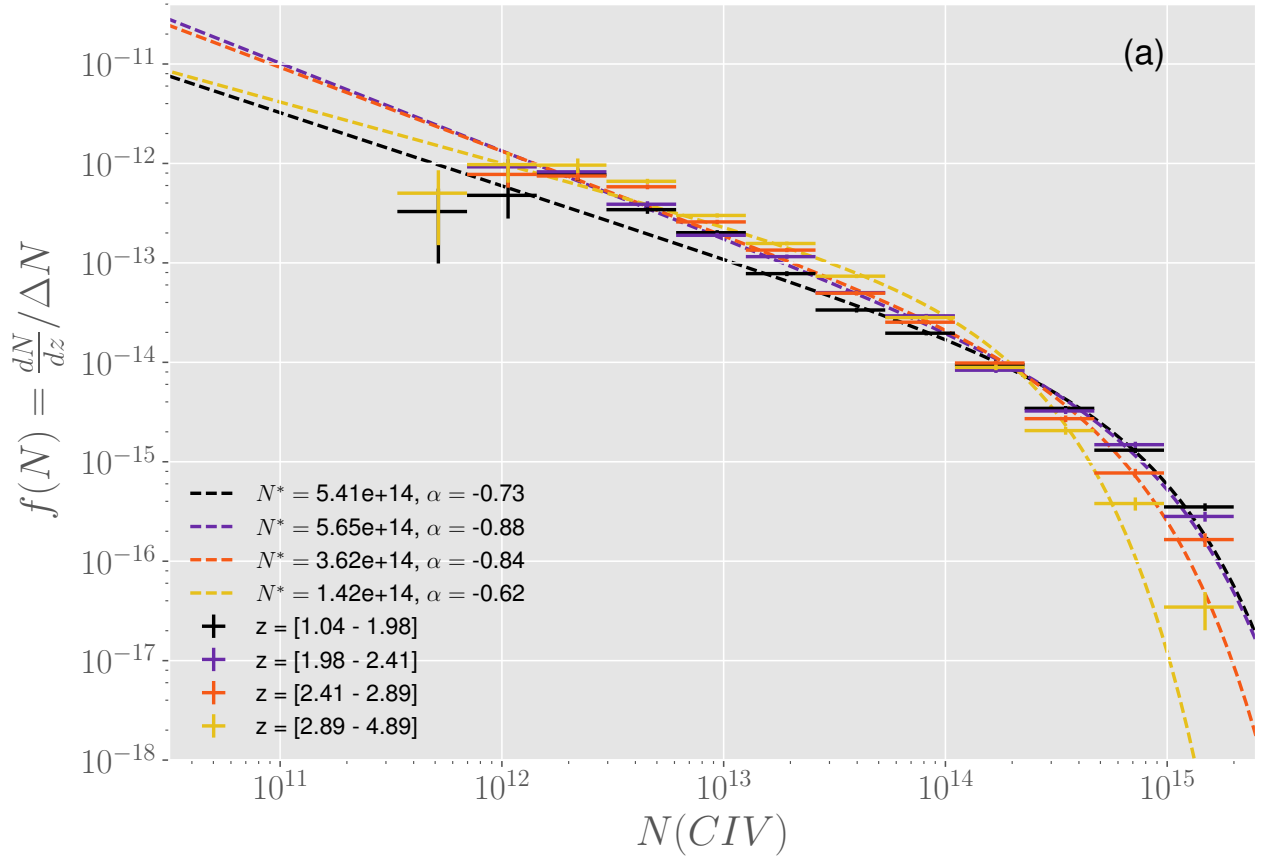
Fig. 6.7.— The column density distribution of C IV absorbers, defined as the comoving line density in each column density bin divided by the bin width. We fit this distribution with a Schechter function.

Fig. 6.8.— The column density distribution of C IV absorbers, defined as the comoving line density in each column density bin divided by the bin width. We fit this distribution with a Schechter function.
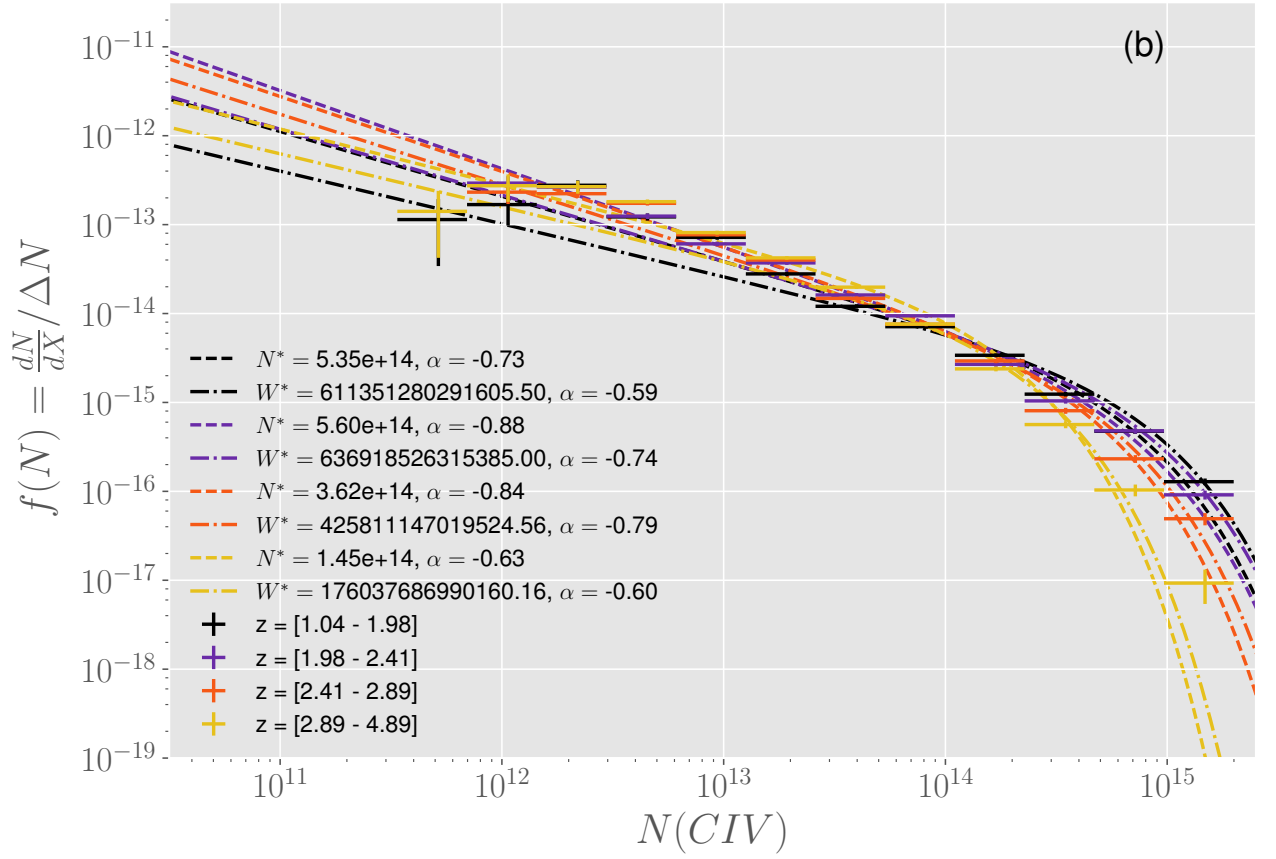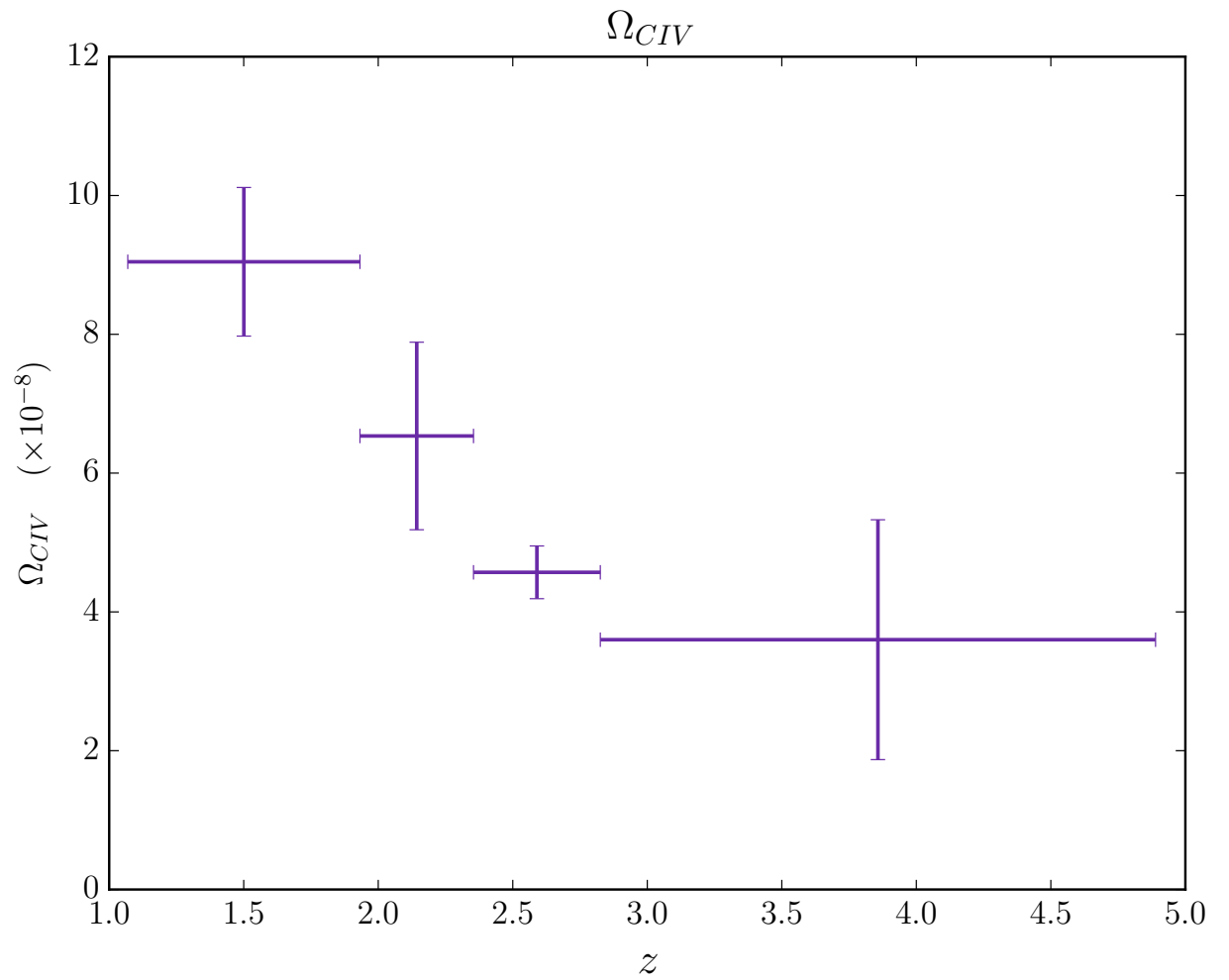
Fig. 6.9.— Ω_{CIV} as a function of redshift. The cosmic mass density of CIV stays roughly flat near a value of 1×10^{-9}, with a potential increase from $z = 0.1$ to $z = 2.5$.

7. KINEMATICS PROPERTIES USING TPCF ANALYSIS

Here we do the whole Nikki thing and interpret the results.

7.1. Mg II Kinematics

Here we slice it, we dice it, and we look at a lot of TPCFs.

7.1.1. Mg II *Redshift Evolution*

Slice with respect to z.

7.2. Mg II Optical Depth Behavior

Slice with respect to tau.

7.3. C IV Kinematics

Here we slice it, we dice it, and we look at a lot of TPCFs.

7.3.1. C IV *Redshift Evolution*

Slice with respect to z.

7.4. C IV Optical Depth Behavior

Slice with respect to tau.

8. CONCLUSIONS

WHAT DOES IT ALL MEAN?!

8.1. Mg II

Long song and dance about how MgII is so great and all.

8.1.1. Strong Absorbers

Talk about all the properties of strong absorbers.

8.1.2. Weak Absorbers

Talk about all the properties of weak absorbers.

8.1.3. Kinematics

Talk about kinematic properties of MgII absorbers.

8.2. C IV

Even longer song and dance about how CIV is arguably even more interesting and important.

8.2.1. Strong Absorbers

Talk about all the properties of strong absorbers.

8.2.2.   Weak Absorbers

Talk about all the properties of weak absorbers.

8.2.3.   Kinematics

Talk about kinematics properties of CIV absorbers.

8.3.   Evolution in the Context of Galaxy Evolution

Evolution.

8.4.   Consequences, and Verification

Consequences.

8.5.   Future Work

This is where my postdoc stuff would go...IF I HAD ONE.

APPENDIX

APPENDIX A.   THERE BE MATH IN THEM THERE HILLS

In this appendix we further explain the line detection technique introduced in Section 3.3. Equations show we can match the filters.

$$P(F,T) = \frac{F}{F_o} - \int_{T_D}^{0} \frac{T}{T_D} dT \tag{A.1}$$

where P is the probability of me giving a Fuck at a given point in time, F is the number of Fucks I currently have, F_o is the total number of Fucks available, T is the current time remaining until a deadline, for a given total given to complete the task, T_D.

A.1.   Appendix subsection

Did you know that this won't show up as listed in the table of contents, in accordance with NMSU thesis policy? Exciting.

REFERENCES

Bordoloi, R., Lilly, S. J., Kacprzak, G. G., & Churchill, C. W. 2014, ApJ, 784, 108

Bordoloi, R., et al. 2011, ApJ, 743, 10

Bouché, N., Hohensee, W., Vargas, R., Kacprzak, G. G., Martin, C. L., Cooke, J., & Churchill, C. W. 2012, MNRAS, 426, 801

Bouché, N., Murphy, M. T., Péroux, C., Csabai, I., & Wild, V. 2006, MNRAS, 371, 495

Chen, H.-W., Lanzetta, K. M., Webb, J. K., & Barcons, X. 2001, ApJ, 559, 654

Chen, H.-W., Wild, V., Tinker, J. L., Gauthier, J.-R., Helsby, J. E., Shectman, S. A., & Thompson, I. B. 2010, ApJ, 724, L176

Chen, S.-F. S., et al. 2016, ArXiv e-prints

Churchill, C. W., Nielsen, N. M., Kacprzak, G. G., & Trujillo-Gomez, S. 2013a, ApJ, 763, L42

Churchill, C. W., Rigby, J. R., Charlton, J. C., & Vogt, S. S. 1999, ApJS, 120, 51

Churchill, C. W., Trujillo-Gomez, S., Nielsen, N. M., & Kacprzak, G. G. 2013b, ApJ, 779, 87

Churchill, C. W., Vogt, S. S., & Charlton, J. C. 2003, AJ, 125, 98

Davé, R., Hernquist, L., Katz, N., & Weinberg, D. H. 1999, ApJ, 511, 521

Ford, A. B., Oppenheimer, B. D., Davé, R., Katz, N., Kollmeier, J. A., & Weinberg, D. H. 2013, MNRAS, 432, 89

Fox, A. J., Ledoux, C., Petitjean, P., & Srianand, R. 2007, A&A, 473, 791

Gauthier, J.-R., Chen, H.-W., & Tinker, J. L. 2009, ApJ, 702, 50

Haardt, F., & Madau, P. 2012, ApJ, 746, 125

Kacprzak, G. G., Churchill, C. W., Evans, J. L., Murphy, M. T., & Steidel, C. C. 2011, MNRAS, 416, 3118

Kacprzak, G. G., Churchill, C. W., & Nielsen, N. M. 2012, ApJ, 760, L7

Lanzetta, K. M., Turnshek, D. A., & Wolfe, A. M. 1987, ApJ, 322, 739

Lovegrove, E., & Simcoe, R. A. 2011, ApJ, 740, 30

Lundgren, B. F., et al. 2009, ApJ, 698, 819

Martin, C. L., & Bouché, N. 2009, ApJ, 703, 1394

Matejek, M. S., & Simcoe, R. A. 2012, ApJ, 761, 112

Matejek, M. S., Simcoe, R. A., Cooksey, K. L., & Seyffert, E. N. 2013, ApJ, 764, 9

Narayanan, A., Misawa, T., Charlton, J. C., & Kim, T.-S. 2007, ApJ, 660, 1093

Nestor, D. B., Johnson, B. D., Wild, V., Ménard, B., Turnshek, D. A., Rao, S., & Pettini, M. 2011, MNRAS, 412, 1559

Nestor, D. B., Turnshek, D. A., & Rao, S. M. 2005, ApJ, 628, 637

Nielsen, N. M., Churchill, C. W., & Kacprzak, G. G. 2013a, ApJ, 776, 115

Nielsen, N. M., Churchill, C. W., Kacprzak, G. G., & Murphy, M. T. 2013b, ApJ, 776, 114

Nielsen, N. M., Churchill, C. W., Kacprzak, G. G., Murphy, M. T., & Evans, J. L. 2015, ApJ, 812, 83

—. 2016, ApJ, 818, 171

Noterdaeme, P., Srianand, R., & Mohan, V. 2010, MNRAS, 403, 906

Oppenheimer, B. D., Davé, R., Kereš, D., Fardal, M., Katz, N., Kollmeier, J. A., & Weinberg, D. H. 2010, MNRAS, 406, 2325

Prochaska, J. X., Weiner, B., Chen, H.-W., Mulchaey, J., & Cooksey, K. 2011, ApJ, 740, 91

Rauch, M., Sargent, W. L. W., & Barlow, T. A. 2001, ApJ, 554, 823

Rubin, K. H. R., Weiner, B. J., Koo, D. C., Martin, C. L., Prochaska, J. X., Coil, A. L., & Newman, J. A. 2010, ApJ, 719, 1503

Rudie, G. C., Steidel, C. C., Shapley, A. E., & Pettini, M. 2013, ApJ, 769, 146

Sargent, W. L. W., Steidel, C. C., & Boksenberg, A. 1988, ApJ, 334, 22

Shull, J. M., Danforth, C. W., & Tilton, E. M. 2014, ApJ, 796, 49

Simcoe, R. A., Sargent, W. L. W., & Rauch, M. 2004, ApJ, 606, 92

Steidel, C. C., Erb, D. K., Shapley, A. E., Pettini, M., Reddy, N., Bogosavljević, M., Rudie, G. C., & Rakic, O. 2010, ApJ, 717, 289

Steidel, C. C., & Sargent, W. L. W. 1992, ApJS, 80, 1

Stewart, K. R., Kaufmann, T., Bullock, J. S., Barton, E. J., Maller, A. H., Diemand, J., & Wadsley, J. 2011, ApJ, 738, 39

Tremonti, C. A., Moustakas, J., & Diamond-Stanic, A. M. 2007, ApJ, 663, L77

Tremonti, C. A., et al. 2004, ApJ, 613, 898

Tumlinson, J., et al. 2011, Science, 334, 948

Tytler, D., Boksenberg, A., Sargent, W. L. W., Young, P., & Kunth, D. 1987, ApJS, 64, 667

Weiner, B. J., et al. 2009, ApJ, 692, 187

Werk, J. K., et al. 2014, ArXiv e-prints

Zibetti, S., Ménard, B., Nestor, D. B., Quider, A. M., Rao, S. M., & Turnshek, D. A. 2007, ApJ, 658, 161